Materials Chemistry and Physics 292 (2022) 126800

Contents lists available at ScienceDirect

Materials Chemistry and Physics

journal homepage: www.elsevier.com/locate/matchemphys

Synthesis of tailored alumina supported Cu-based solids obtained from nanocomposites: Catalytic application for valuable aldehyde and ketones production

José Vitor C. do Carmo [a], Rita de Cássia F. Bezerra [a], Samuel Tehuacanero-Cuapa [b], E. Rodríguez-Aguado [c], Rossano Lang [d], Adriana F. Campos [e], Gian Duarte [e], Gilberto D. Saraiva [f], Larissa Otubo [g], Alcineia C. Oliveira [a,*], E. Rodríguez-Castellón [f]

[a] Universidade Federal do Ceará, Campus do Pici, Bloco 940, Departamento de Química Analítica e Físico-Química, 60455-760, Fortaleza, Ceará, Brazil
[b] Instituto de Física, UNAM, Circuito de la Investigación s/n, Ciudad Universitaria, 04510, Coyoacán, D. F., Mexico
[c] Universidad de Málaga, Departamento de Química Inorgánica, Facultad de Ciencias, 29071, Spain
[d] Instituto de Ciência e Tecnologia, Universidade Federal de São Paulo– UNIFESP, São José dos Campos – SP, Brazil
[e] Centro de Tecnologias Estratégicas do Nordeste, CETENE, Av. Prof. Luís Freire, 1 - Cidade Universitária, Recife, Pernambuco, 50740-545, Brazil
[f] Faculdade de Educação Ciências e Letras do Sertão Central, Universidade Estadual do Ceará, Quixadá, Brazil
[g] Centro de Ciência e Tecnologia de Materiais - CCTM, Instituto de Pesquisas Energéticas e Nucleares - IPEN, 05508-000, São Paulo, Brazil

HIGHLIGHTS

- Tailored CuO–ZnO/Al_2O_3 catalyst obtained from CuZnAl@C nanocomposite.
- Simple sonochemical route via core/shell assisted by reverse micelle synthesis.
- Nuclei composed of Cu and Zn domains coated by a semi-crystalline lauric acid-based shell.
- Highly dispersed CuO and ZnO on alumina converting ehtylbenzene.

GRAPHICAL ABSTRACT

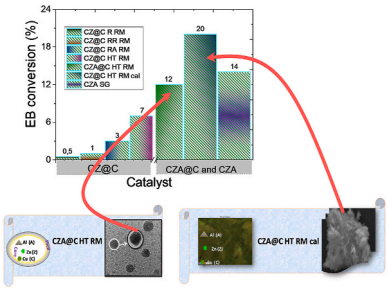

ARTICLE INFO

Keywords:
Porous alumina
Nanocomposites
CuZnAl@C
Cu-based nanomaterials
Oxidation

ABSTRACT

A tailored nanostructured CuO–ZnO/Al_2O_3 catalyst was obtained from nanocomposites via sonochemical route through core/shell assisted by reverse micelle synthesis. The as-synthesized nanocomposites consisted of Cu, Zn and Al domains coated by a lauric acid shell structure with controlled physicochemical properties. Combining these features, a porous CuO–ZnO/Al_2O_3 supported catalyst was obtained from CuZnAl@C nanocomposite, in which Cu and Zn oxide nanoparticles interacted quite strongly with alumina. In this study, a nanostructured CuO–ZnO/Al_2O_3 was applied to oxidize ethylbenzene in the presence of H_2O_2. Catalytic results further demonstrated that the nanostructured solid had ethylbenzene conversion superior to 20% and good selectivities to acetophenone, benzaldehyde and benzoic acid compared to a benchmark CuZnAl catalyst obtained by the sol-gel method.

* Corresponding author.
E-mail address: alcineia@ufc.br (A.C. Oliveira).

https://doi.org/10.1016/j.matchemphys.2022.126800
Received 23 June 2022; Received in revised form 30 August 2022; Accepted 16 September 2022
Available online 23 September 2022
0254-0584/© 2022 Elsevier B.V. All rights reserved.

1. Introduction

Cu-based materials have received much interest in the past decades because of their high potential as catalysts, adsorbents and sensors [1–4]. In this sense, alumina-supported Cu-based solids are a relatively new class of engineered supported catalysts, which have been investigated for catalytic applications in alkylaromatic oxidation reactions [5–10].

The CuO–ZnO/Al_2O_3 supported catalyst has driven numerous investigations in industrial catalyst preparation to improve the outcome of the easy aggregation of Cu(II) and Zn(II) oxides particles [7,11–14]. Thus, the sintering process has still stunted the application of bare CuO–ZnO/Al_2O_3 commercially available catalyst causing a decrease of its stability in the catalytic reactions [11,12].

Particularly, to our best knowledge, a variety of preparation methods have been developed on new CuO–ZnO/Al_2O_3 catalysts, including traditional co-precipitation, pyrolysis, sol-gel, microemulsion, core-shell and mechanical mixtures to improve their physicochemical properties [11–16]. Although CuO–ZnO/Al_2O_3 has been successfully prepared via the aforesaid methods, the good dispersion of stable Cu(II) and Zn(II) oxide nanoparticles on alumina surface has proved to be more challenging owing to the disadvantages of such methods in facilitating the general tendency to aggregate these nanoparticles on the alumina surface, especially for co-precipitation [13,14].

Based on these concerns, studies on preparation methods of these catalysts already exist, but they include expensive instrumentation and reactants that are not readily available in most laboratories. Hence, there is still a great need for a reliable synthesis route to disperse ZnO and CuO nanoparticles on the surface of alumina-based catalysts.

In the case of alkylaromatic oxidation reactions, the selective oxidation of ethylbenzene either in the presence of hydrogen peroxide or oxygen has been investigated for the production of valuable compounds such as acetophenone, benzyl alcohol and benzaldehyde [9,17,18]. The CuO–ZnO/Al_2O_3 catalyst is particularly interesting for the selective oxidation of EB (Fig. 1). This is due to the fact of the Cu^{2+}/Cu^{+} interaction with Zn and Al oxides in the presence of oxidants could accelerate the reaction. Thus, the subsequent reaction chains and the benzaldehyde, benzoic acid and acetophenone products can be obtained through the free-radical chain mechanism [9,17].

Although several attempts have been made to improve the properties of CuO–ZnO/Al_2O_3 catalysts, the sintering of the particles is the main drawback to obtain good catalytic performance in the oxidation reactions.

In this paper, a simple sonochemical method to synthesize nanostructured CuO–ZnO/Al_2O_3 via core/shell assisted by reverse micelle route is investigated. Motivated by the need to prepare efficient alumina supported catalysts, the improvement of physiochemical properties of CuO–ZnO/Al_2O_3 is achieved via the aforesaid route, compared to that of sol-gel method.

Synthetically, alternative hybrid organic/inorganic syntheses routes to modulate surface morphology of the solid allow a broad range in crystallite size variation of the Zn(II) and Cu(II) oxide nanoparticles together with an excellent dispersion of the oxides on alumina. Indeed, the resulting nanostructured CuO–ZnO/Al_2O_3 synthesized by the combined sonochemical-core/shell assisted by reverse micellization approach possesses distinct physicochemical features providing stable particles with sizes of several tens of nanometers.

Lastly, the main objective of the present work would be at least that the screen the best route, but more significantly, it seeks to elucidate the structural, morphological and surface properties correlations with the catalytic activity of nanocomposites.

2. Experimental

2.1. Combined sonochemical-core/shell synthesis assisted by reverse micelle method

The CuO–ZnO@C, denoted as CZ@C nanocomposites, was primarily synthesized as precursors to choose the most appropriate method to obtain the CuO–ZnO–Al_2O_3@C *i.e.,* CZA@C nanocomposites. The combined sonochemical-core/shell method assisted by reverse micelle method with using various approaches was applied in all synthesis routes investigated. Finally the CuO–ZnO/Al_2O_3 solid was obtained from the CZA@C nanocomposites.

In the first stage, the nanocomposites were synthesized by dispersing 0.003 mmol of polyethylene glycol (PEG, $H(OCH_2CH_2)_nOH$) and 3.42 mmol of polyvinylpyrrolidone (PVP, $(C_6H_9NO)_n$ with an average molecular weight of 40.00 g mol^{-1}) in 8 mL of absolute ethanol (C_2H_5OH, 99.5%) and 1 mL of aqueous sodium hydroxide 0.1 mol L^{-1} solution under vigorous stirring at room temperature for 0.5 h. After this period, a 2.3 mmol of zinc acetate dihydrate ($Zn(CH_3COO)_2{\bullet}2H_2O$) solution was first mixed with 1.8 mmol of copper(II) nitrate trihydrate ($Cu(NO_3)_2{\bullet}3H_2O$, 99%) solution and slowly added to the previous mixture to form the so called solution I. This solution was then aged under constant stirring at 40 °C for 0.5 h.

Simultaneously, a 1.37 mol of cetyltrimethylammonium bromide (CTAB, $CH_3(CH_2)_{15}N(Br)(CH_3)_3$ 98%) surfactant solution and 1.5 mmol of lauric acid ($CH_3(CH_2)_{10}COOH$, 98%) were dispersed into 25 mL of distilled water under heating and the resultant solution was submitted to microwave irradiation at 50 mW for 3 times at intervals of 10 s to obtain solution II. The product was a dark greenish transparent suspension, which was reserved for further treatments.

In the second stage, both solution I and solution II were mixed, sonicated and submitted to five distinct treatment routes, as follows:

(i) aging solutions I and II at room temperature for 2 h and then, the mixture was refluxed at 80 °C for 2 h to form the as-synthesized CZ@C R RM sample;
(ii) refluxing solution I at 80 °C and then aging at room temperature for 2h with a subsequent addition of solution II followed by second round of refluxing and aging during 2 h to obtain the as-synthesized CZ@C RR RM sample;
(iii) submitting solution I to reflux at 80 °C during 2 h and afterwards the mixture was aged at room temperature. Then, solution II was added to the previous mixture and stirring was continued for

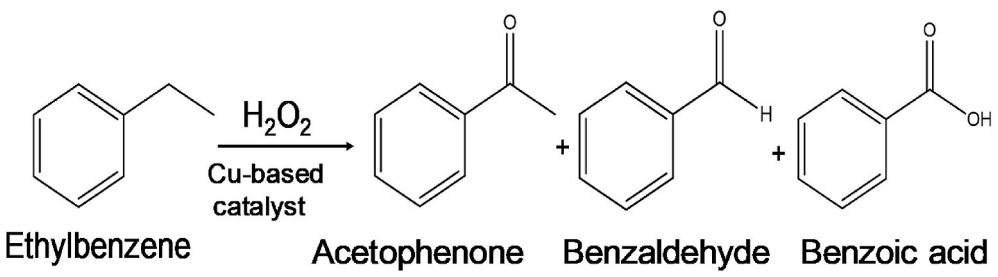

Fig. 1. Schematic illustration of the EB oxidation reaction in the presence of H_2O_2 as oxidant.

additional for 6 h to obtain the as-synthesized CZ@C RA RM sample;

(iv) stirring solutions I and II at room temperature for additional 30 min and subsequently, the mixture was submitted hydrothermal treatment in a Teflon-lined autoclave and held at 80 °C for 24 h an oven. The hydrothermal treatment aims to obtain a specific morphology through dissolving and recrystallizing the insoluble substances in aqueous solution under autogenous pressure to obtain the as-synthesized sample CZ@C HT RM;

(v) stirring solution I with a 1.0 mmol of aluminum nitrate nonahydrate ($Al(NO_3)_3 \bullet 9H_2O$,98%) solution and after that adding solution II at room temperature for additional 30 min. The mixture was placed into a Teflon-lined autoclave in an oven and held at 80 °C for 24 h yielding the as-synthesized CZA@C HT RM sample. Afterwards, the light greenish paste was washed with deionized water and then, dried overnight at 60 °C to remove residual traces of the adsorbed compound. Finally, the as-synthesized CZA@C HT RM solid was calcined using an analogous procedure at 300 °C with a heating rate of 1 °C min^{-1} during 2 h to obtain CZA@C HT RM cal sample.

To summarize, after sonication of the prepared solutions I and II, distinct techniques *i.e.,* reflux, double reflux steps, reflux followed by aging and hydrothermal treatment were applied to the solutions to obtain the CZ@C precursors with nominal composition of Cu/Zn of 1.0:1.0. Then, a suitable methodology was chosen to obtain CZA@C RM nanocomposite from the CZ@C precursors.

The letters C, Z and A mean copper, zinc and aluminum, respectively. The abbreviations R, RA, RR, HT, RM and RM cal indicate, reflux and reflux accompanied by aging, two times refluxed, hydrothermal treatment reverse micelle, reverse micelle method followed by calcination.

The description of the performed synthesis routes is illustrated in Fig. S1 (Fig. S1, supplementary material Scheme I and Scheme II).

2.2. Catalyst synthesis by sol-gel method

The traditional sol-gel method was used to synthesize a reference CZA solid. Details of the synthetic method were given in previously reported procedures with modifications [19]. In a typical synthesis, 3.6 mmol of aluminum tri-sec-butoxide ($Al(O\text{-}sBu)_3$, 99%) diluted in 3.25 mmol of absolute ethanol and 4.15 mmol of copper(II) nitrate solution were vigorously stirred for 1 h. After stirring the obtained suspension, the xerogel, was refluxed at 100 °C for 1 h.

Then, about 25 mL of nitric acid solution for peptization was added to the slurry and the pH was adjusted. Subsequently, the slurry was stirred again with 4.05 mmol of zinc acetate solution and refluxed during 1 h and the gel formed was thoroughly washed with deionized water. The solution was then centrifuged to remove the excess of the organics and nitrates. After that, the gel was oven dried at 70 °C for 24 h. Finally, the resulting gel was calcined at 300 °C with a heating rate of 1 °C min^{-1} during 2 h under flowing air to produce the supported $CuO–ZnO/Al_2O_3$ reference catalyst. The final solid was designated as CZA SG.

All reagents were purchased from Sigma-Aldrich and used as received without any further purification.

A schematic illustration of the synthesis method of the CZA nanocomposite was summarized in Fig. S1 (Fig. S1, Schema III).

2.3. Characterizations

X-ray diffraction (XRD) patterns were measured on a DMAXB Rigaku diffractometer with Cu-Kα radiation (1.5406 Å) at 40 kV and 25 mA. The diffractograms were recorded in the 2θ values with a 0.02 ° step per 100 s using a Bragg-Brentano geometry. The diffraction patterns were compared to those of the JCPDS (Joint Committee of Powder Diffraction Standard). The crystallite sizes were estimated by applying the Scherrer equation for lauric acid structure of the CZ@C nanocomposites.

Fourier transform infrared spectroscopy (FTIR) measurements were carried out on a Bruker Vertex 70V FT-IR spectrometer. Prior to the measurements, samples were diluted in dried KBr using a ratio of 1:100 for sample: KBr. Then, the mixture was ground to form the FTIR the pellets. The FTIR curves were acquired at spectral range of 4000-400 cm^{-1} with a resolution of 4 cm^{-1}.

Scanning electron microscopy (SEM) images were recorded using a FEI, Quanta 200 FEG electron microscope equipped with an Energy Dispersive Spectroscopy (EDS) system, which operates at 2 kV accelerating voltage. Before the analyses, the samples were sputtered with a thin gold film to improve the conductivity.

Raman measurements for selected samples were performed on a LabRAM HR Horiba Scientific spectrometer using an objective lens of 50 times. The 785 nm laser line was applied on solids to excite the Raman spectrum at 2 mW. The spectra were obtained in the 200–1800 cm^{-1} range with a resolution of 4 cm^{-1} with 8 accumulations per second for each spectrum.

Transmission electron microscopy (TEM) micrographs were recorded for selected samples using a FEI TECNAI G2 20 high-resolution transmission electron microscope operating at 200 kV. Before analyses, samples were suspended in a few drops of ethanol and subsequently, sonicated for a few minutes. Finally, the samples were deposited onto the gold grids covered with holey carbon support films.

X-ray photoelectron spectroscopy (XPS) analyses were performed on a Physical Electronics VersaProbe II Scanning XPS Microprobe. The data were acquired by using a scanning monochromatic Al-Kα X-ray radiation and a charge neutralizer operating at a vacuum better than 10^{-7} Pa. Binding energies were referenced to the adventitious carbon with C 1*s* at 284.8 eV.

Nitrogen adsorption–desorption isotherms were measured at liquid nitrogen temperature on an ASAP 2420 (Micromeritics), after desorbing the samples at 150 °C for 8 h. The surface area and the pore size distribution were calculated by the Brunanuer, Emmett and Teller (BET) equation and Barrett Joyner Halenda (BJH) model, respectively. Micropores areas were determined by the *t*-plot method.

2.4. Catalytic activity tests in ethylbenzene oxidation in the presence of H_2O_2

The liquid phase catalytic evaluation was carried out in a batch glass reactor equipped with a refluxed condenser and a water bath. About 50 mg of catalyst were filled in the reaction together with 1 mmol of ethylbenzene ($C_6H_5C_2H_5$ anhydrous, 99.8%), 1 mmol of hydrogen peroxide (H_2O_2 30 wt.% in water) and acetone (CH_3COCH_3 99.0%) as solvent. The reaction system was magnetically stirred and coupled to the thermocouple at 50 °C to eliminate the diffusion effect for 6 h under constant stirring. After centrifugation of the used catalyst, the reaction products were analyzed by gas chromatography using a flame ionization detector (FID). The conversion and selectivity were calculated as described in earlier works [15,16].

3. Results and discussion

3.1. Structure of the CZ@C nanocomposites through XRD, Raman and FTIR spectroscopy

Characteristic of a typical semicrystalline structure, the CZ@C precursors (Fig. 2A) depict the main diffractions peaks at around 2θ = 6.6 (200), 8.7 (300), 16.7 (500), 20.4 (310), 21.3 (211), 23.8 (402), 29.9 (412) and 40.0° (304). These reflections are indexed to be from the crystal structure of lauric acid in all samples (JCPDS file 038–1976). Other peaks arising at 2θ = 7.9 (020), 19.9 (207), 23.8 (411) and 24.4° (600) are in a similar position to reflections of the lauric acid structure (JCPDS file 008–0664), as found elsewhere [20]. The positions of the main peaks could indicate that the monoclinic structure of lauric acid

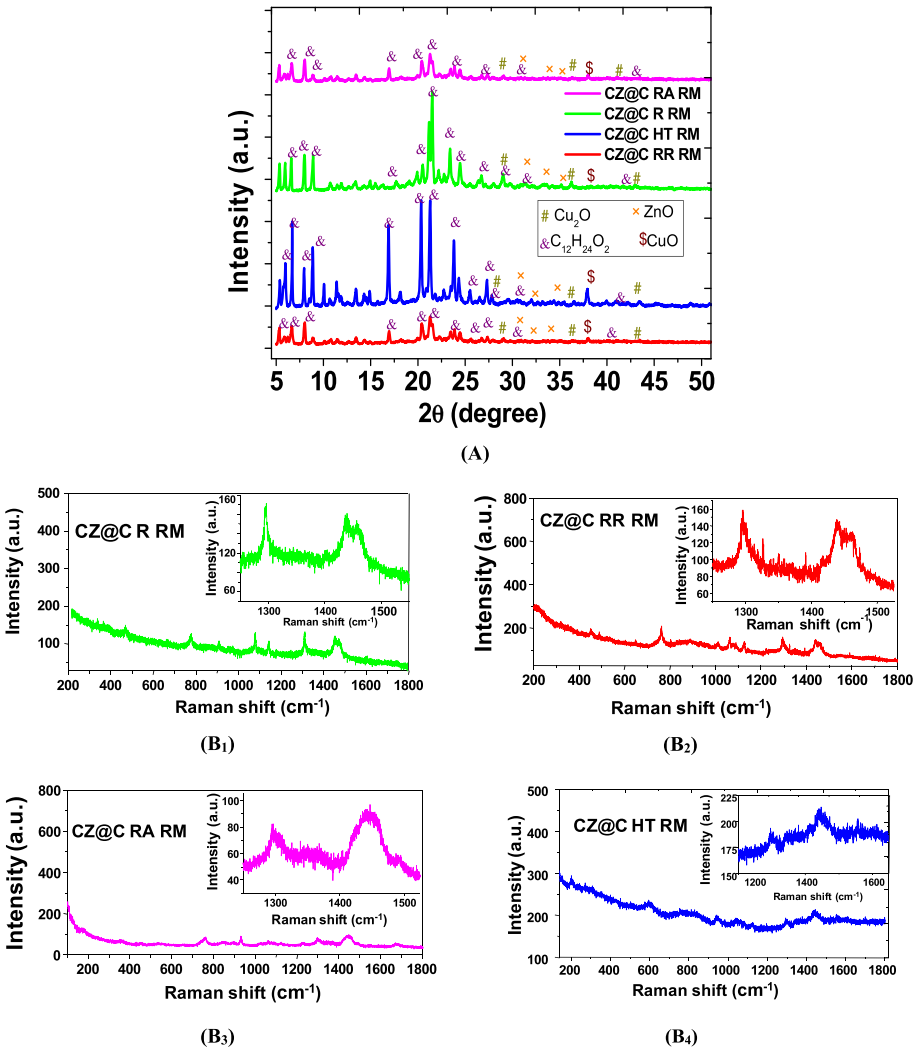

Fig. 2. (A) Structure by XRD and (B) Raman measurements of the CZ@C nanocomposites obtained by combined-sonochemical core/shell synthesis assisted by reverse micellization method.

may be present, which matches well with the values reported for bulk lauric acid [21].

Important is to note that some diffraction peaks clearly illustrate the presence of the cubic *fcc* Cu_2O phase at 2θ position of 28.9 (110), 36.3 (111) and 42.7° (200), based on JCPDS file 05–0667. Moreover, PVP and PEG act as chelant agents for divalent cations resulting in the reduction of Cu^{2+} ions to Cu^{+} e.g., Cu_2O and metallic Cu as well [22]. At 2θ position of 38.7° (111), the lattice plane can be assigned to the monoclinic CuO phase coexisting with Cu_2O, in line with the findings [22]. Furthermore, weak reflections can be readily indexed to be from poorly crystallized ZnO wurtzite hexagonal structure at 2θ = 31.3 (100), 33.4 (002) and 35.7° (101), in agreement with the JCPDS file 36–1451 [23]. Together CuO, Cu_2O and ZnO phases represent 3% of the phases, being lauric acid the prevalent phase in the CZ@C precursor nanocomposites. Additionally, the broad and weak reflections of the aforesaid CuO and ZnO phases indicate that their sizes are too small to generate strong diffraction lines. Also, the CuO and ZnO oxides may be located in a core coating by lauric acid and other organics shell or yet, the metal oxide can be incorporated to lauric structure, since the synthesis processes do not lead to structural changes in lauric acid structure.

The sonochemical route has been thoroughly developed for preparing small nanoparticles either on nanocasted metal oxide surfaces or within of its pores [24,25]. Therefore, sonication furnishes energy to boost Zn^{2+} and Cu^{2+} ions toward PVP and lauric acid organic stabilizers to facilitate binding between metals and carbon sources. Although PVP and lauric acid stabilizers are not dissolved to obtain hydrophilic-soluble species such as ethanol and water, at a pH of 10 upon NaOH addition to solutions, sonication affords the production of negatively charged carboxyl and amides free radicals in solution. Upon impact, these species react to chelate the positively charged Cu(II) and Zn(II) ion precursors and further result in the formation of Me–O–C bonds. As a result, reverse micelles are formed due to the help of CTAB surfactant and lauric acid radicals consisting of a microemulsion along with PVP and PEG organic stabilizers form a shell, which chelates with metal oxide species into the nuclei.

After sonication, the mother solutions were submitted to distinct procedures. In the case of refluxing after sonication, the synthetic route is achieved by the formation of a dark bluish color of the as-prepared CZ@C R RM sample. The aforesaid color indicates that entire Cu^{2+} nanoparticles reduction does not occur in solution during the combined sonication and reflux. After gel formation and subsequent growth, the copper and zinc nanoparticles are probably coated by the outer carbon shell originated from the organic stabilizer and lauric acid, as well.

Notably, the single step of reflux treatment in the CZ@C R RM sample allows for much stronger peak intensities than the CZ@C RR RM sample (Fig. 2A), which is synthesized through double reflux treatment. This is an indicator of the cation ordering of Cu(II) and Zn(II) with the alkyl chain of lauric acid, CTAB, PEG and PVP in ethanol and sodium

hydroxide media under a sonochemical mechanism. Upon only one evaporation and condensation step of reflux of the previous solution, the final solid structure is affected in terms of crystallinity. In this regard, the surfactant-assisted reaction among PEG, PVP, lauric acid and CTAB provide the formation of the micelles around the divalent cations. Simultaneously, control of the nucleation and growth of particles is governed by the aforesaid surfactant molecules, which modulate kinetics and determine particles sizes. As a consequence of the divalent cations being slowly released from the micelles, they may form large particles with improved crystallinity of lauric acid peaks, as observed in PVP and CTAB assisted syntheses of nanocomposites [26]. Accordingly, the Scherrer's equation is used to estimate the crystal sizes of the solids for the (211) reflection, which is 12 nm for the CZ@C R RM nanocomposite.

On the contrary, a double reflux step may cause the release of divalent cations from the micelles more quickly, limiting the particle growth resulting in low particles and thereby, lower intensity peaks in the XRD diffractogram (Fig. 2A). Bearing these observations in mind, the intensity of the XRD peaks of CZ@C RA RM is weaker than that of CZ@C R RM due to the reflux step accompanied by aging of the former nanocomposite solution allowing the formation of more micelles and thus, more nuclei of particles with the consequent nanocrystal growth enhancement.

Additionally, the combination of sonochemical and double reflux techniques has produced a dark blue-black color of as-synthesized CZ@C RR RM sample giving direct evidence that double reflux forms small metal oxides particles coated by carbon species, as seen through the low intensity of the diffraction peaks. These evidences are later assessed by SEM-EDS images.

Remarkably, the XRD peaks of the hydrothermally treated CZ@C HT RM nanocomposite are more intense than the other samples (Fig. 2A). The hydrothermal treatment step allows the use of low temperatures for the stabilization of either anhydrous oxides suspensions or colloids [19,27]. Thus, large crystallite sizes of the particles can be produced upon applying hydrothermal treatment to PEG and PVP modifiers along with the use of reverse surfactant CTAB and lauric acid micelles microemulsion under autogenous pressure. This may provide easy crystallization and further agglomeration of particles, as suggested by the high XRD peak intensities of the CZ@C HT RM nanocomposite. Accordingly, the CZ@C HT RM has the largest crystal size of ca 25 nm among the samples studied.

Raman measurements of selected CZ@C nanocomposites are performed (Fig. 2B) to correlate the structural changes of the CZ@C nanocomposites synthesized by distinct approaches.

All samples depict weak and broad bands that are detected below 200 cm^{-1}, which may be associated with either the O–O bonds stretchings of the two adjacent carboxylic heads of the H-bonded lauric acid dimmers or C–C vibration modes or the paraffinic skeleton of lauric acid [28]. In the medium wavenumber regions, all samples exhibit weak Raman bands around 330 and 758 cm^{-1}, which are assigned to C–C bonds. Two strong bands at about at 890 and 905 cm^{-1} are due to $\rho(CH_2)$ rocking modes. Moreover, a triplet is observed at around 1060, 1075 and 1120 cm^{-1}, which is attributed to the νC-C of the paraffinic chain of lauric acid, especially in CZ@C R RM and CZ@C RR RM (Fig. 2B_1 and Fig. 2B_2).

Also, the stretching modes and strong bands between 1400 and 1500 cm^{-1} consist of the $\delta(CH_2)$ scissoring mode from lauric acid, along with the contribution of the CH_3 mode in the 1500-1650 cm^{-1} range that are vividly observable at high wavenumbers ranges (Fig. 2B, included in all solids). These results evidence the XRD measurements that confirm the presence of lauric acid in all CZ@C nanocomposites, independently of the synthetic route used.

Additionally, the appearance of weak Raman modes observed at 310, 413 and 640 cm^{-1} suggests that the cubic Cu_2O phase is present in all solids, in good agreement with the XRD patterns. Indeed, Cu_2O belongs to the O_h^4 space group (*Pn3m* point group) with two formula units per primitive cell and there are normally six zone centers of optically active phonons out of which two are IR active [29]. These modes arise in the wavenumbers regions close to 348 Bg, 630 and 1122 cm^{-1} corresponding to the CuO, which belongs to the C_{2h}^6 space group with two species per primitive cell.

It is worth highlighting that the fairly narrow Raman modes of the Zn–O bonds can be suggested at around 440 and 570 cm^{-1}. The hexagonal ZnO wurtzite-crystal structure belongs to the space group *P6₃mc* (C_{6v}^4) with two formula units per primitive cell with two A1, two E1 and two E2 Raman active modes [30]. Hence, the modes at 440 and 570 cm^{-1} are assigned to ZnO optical phonons, whereas the Raman bands from 1150 to 1450 cm^{-1} are associated with the optical overtones of the second-order Raman active modes, particularly in CZ@C RA RM and CZ@C HTRM (Fig. 2B_3 and Fig. 2B_4). These results are in line with those reported for the nanostructured ZnO catalyst [30] and agree with the XRD results.

The functional groups observed by FTIR spectra of the as-synthesized CZ@C nanocomposites (Fig. S2) are in good agreement with those observed by Raman measurements. The attribution of the FTIR absorption bands for the nanocomposites is depicted in Table 1. Summarizing, FTIR bands are dominated by absorption bands at about 3340 and 1610 cm^{-1} for all solids, being typically associated with O–H vibrations of adsorbed water molecules [31,32]. The CH_3 vibration appears at around 2929 and 2850 cm^{-1} coming from the CTAB, PVP and lauric acid [30–32]. The νC=O stretching of the pyrrolidone rings arises at about 1703 cm^{-1} while carboxylates coming from PVP and lauric acid appear at 1580 and 1427 cm^{-1}. Also, the C–N vibration of the amide group of PVP is visible at 1240 cm^{-1}. The C–H rocking vibration of lauric acid arises at 692 cm^{-1}. Below 980 cm^{-1}, the Me–O bonds (Me = Cu or Zn) can be identified as not well-defined bands.

3.2. Morphology and texture of the CZ@C precursors of the nanocomposites

The surface morphologies of the *CZ@C* precursors are illustrated in Fig. 3. The morphology of the CZ@C R RM nanocomposite illustrated by the SEM micrograph is found to be platelets (Fig. 3A_1 top left) on which uneven nanoparticles are dispersed (Fig. 3A_2 EDS image, top right).

When the sonicated lauric acid and CTAB are added to the aforesaid reflux system, the microemulsion is formed. It consists of reverse micelles systems that allow chelating of the metals to obtain a plate-like layer upon drying of the solid, in which the Cu and Zn nanoparticles

Table 1
The assignments of the FTIR bands of solids in study compared with the literature reports.

Vibration type		Frequency (cm^{-1})	References (cm^{-1})
νO-H	free	3500	3600 [30,32]
	structural	3340	3400 [30,32]
δO-H	deformation	1610	1600 [30,32]
C-H	$\nu CH_{3\ as}$	2929	2918 [32–34]
	$\nu CH_{3\ s}$	2850	2856 [33,34]
	νCH_2	2848	2850 [32–34]
	δCH_3 and δCH_2	1468–1405	1500-1400 [33]
νC=O	carboxyl group	1703	1700 [33,34]
$\nu_{as}COO^-$	assymmetric stretching	1580	1550 [32,33]
ν_sCOO^-	Symmetric stretching	1427	1390 [32,33]
νC-N	stretching vibration	1207	1200
νC-O	stretching vibration	1085	1100
Me–O; Me–O–Me (Cu, Zn)	scissoring, wagging and twisting metal-oxygen bonds	980 540 and 430	<900 [20,32]
νCH_3COO^-	scissoring vibration	–	690
ρCH_2	rocking	692	710
νAl-O	boehmite	890, 721, 623 and 480	884, 740, 621 and 479 [32]
δAl-OH	boehmite	1069	1072 [20]

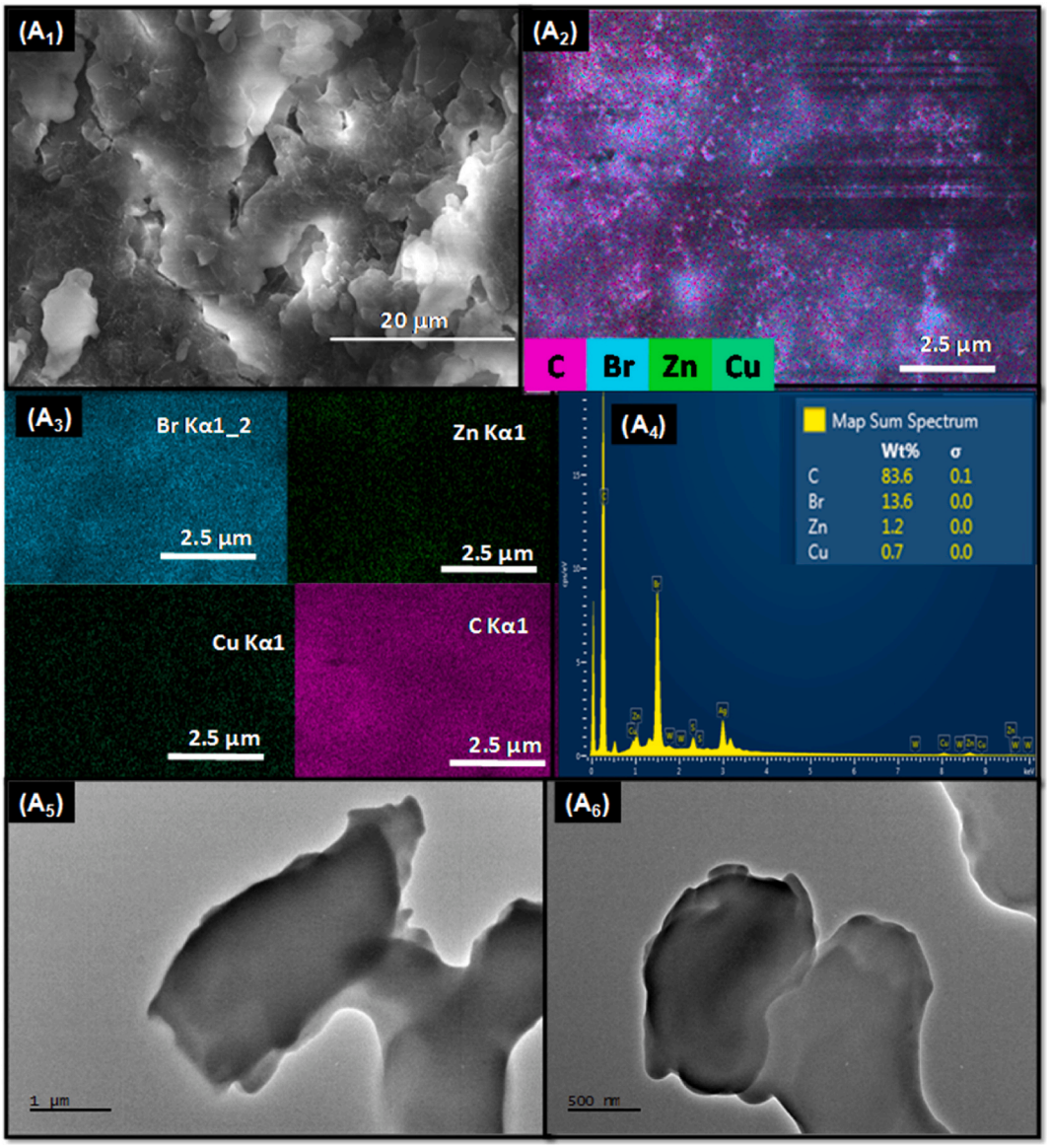

Fig. 3. Surface morphology by SEM-EDS of the CZ@C nanocomposites prepared by combined sonochemical-core/shell synthesis by reverse micelle method: (A) CZ@C R RM, (B) CZ@C RR RM, (C) CZ@C RA RM and (D) CZ@C HT RM. The letters C, Z and A mean copper, zinc and aluminum, respectively. The TEM images of CZ@C R RM nanocomposite are included.

are fairly observable. Moreover, the reflux step gives the Cu and Zn metal oxide particles control of the core dimension and the dispersion of these nanoparticles on the platelets, as seen in EDS mapping. Indeed, the percentages of Cu and Zn on solid surface are 1.2 and 0.7 wt%, being carbon from the shell mostly present (EDS spectra in Fig. 3.A_3 center left and Fig. 3A_4 center right).

These observations corroborate FTIR and Raman results that exhibited carbon vibrations from the lauric acid structure and suggest that the oxides are mostly present on the outer surface of the solid *i.e.,* shell. Moreover, residual Br coming from the CTAB surfactant is observed in all solids studied. TEM images of CZ@C R RM show aggregated particles without a defined morphology (Fig. 3A_5, bottom left). A closer look in the TEM micrograph (Fig. 3A_6, bottom right) suggests that some regions are composed of a dark area representing a core from metal oxide species, which is indeed involved by a clear leaf shaped shell from carbon. This could be an indication of a disordered core-shell structure upon reflux is formed, in line with XRD results.

It is clearly visible that the shape of the particles is not significantly affected by the double reflux step in the SEM micrograph of CZ@C RR RM (Fig. 3B_1, top left). Instead, the plates became more aggregated and their surface smoothed out. It seems that double reflux step facilitates close contact and strong interaction between the metal oxide species and organic compounds. However, the consecutive reflux steps result in a non-uniform distribution of C, Cu, Zn, Br and O elements on the solid surface, as depicted in the EDS image and mapping (Fig. 3B_2 top right and Fig. 3B_3 bottom left). Accordingly, an increase in the Cu and Zn amounts on the solid surface of ca. 2.6 and 4.7 wt% are observed in the EDS spectrum (Fig. 3B_4 bottom right). Furthermore, the double reflux also modulates the crystal sizes decrease, in accordance with the XRD patterns.

Likewise, the SEM micrograph of CZ@C RA RM depicts a plate with grooves and tidily aggregated particles with voids on the plate (Fig. 3C_1 top left). It is interesting to note that the synthesis conditions gives a gel comprising the organic compounds, structure directing agent, lauric acid and metals that are refluxed. This route is accompanied by a subsequent aging step forming many individual nuclei, mostly aggregated

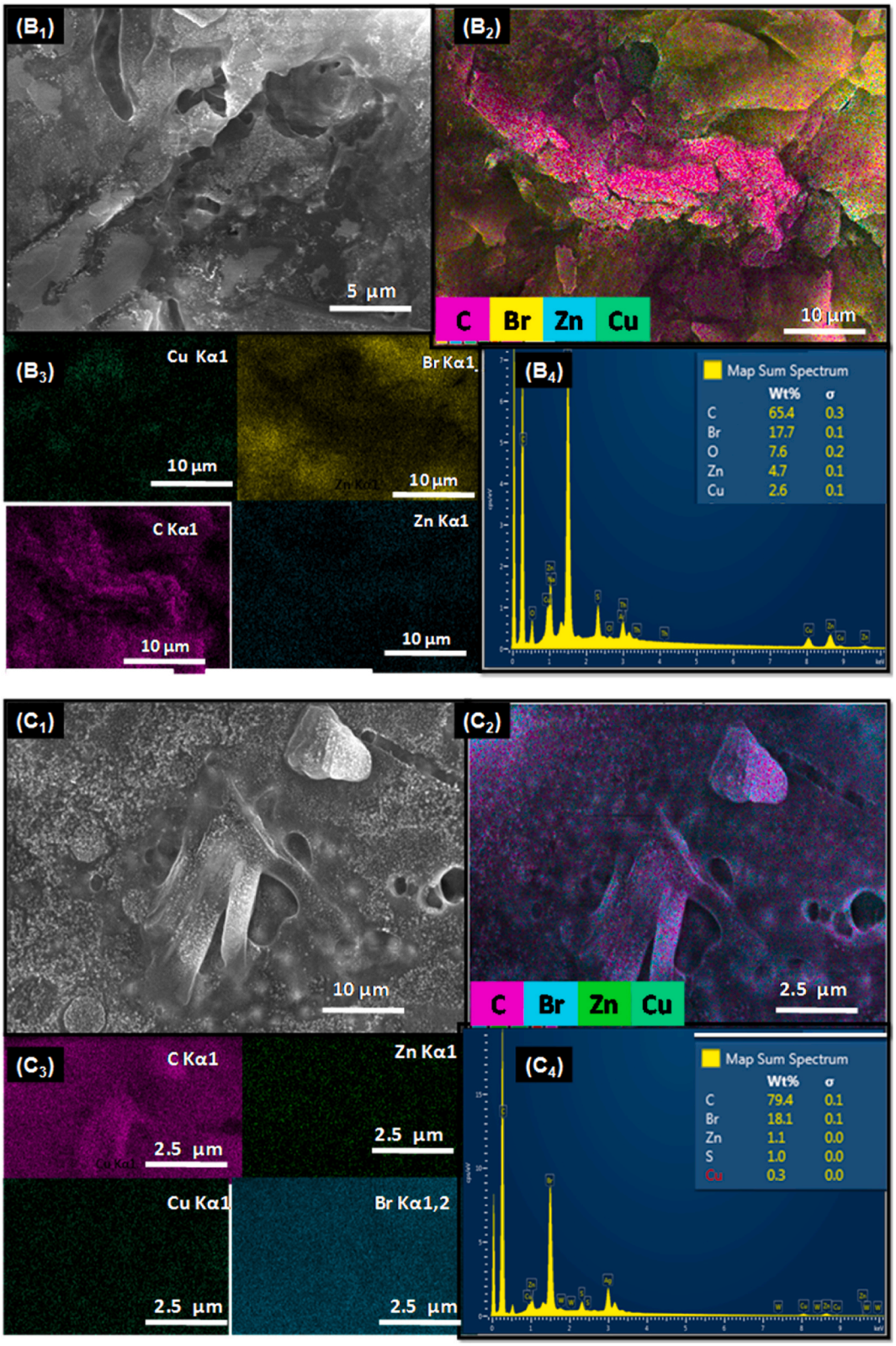

Fig. 3. (*continued*).

due to the crystallization to give nanocrystallites during the initial stages of synthesis. Accordingly, the reflux accompanied by aging may lead to poorly crystallized material as observed in XRD results. In addition, some of these nanoparticles are composed of C, Zn, Br and O elements on a solid surface (Fig. 3C_2 top right) with a low amount of Cu, as seen in the EDS mapping and spectrum of CZ@C RA RM (Fig. 3C_3 bottom right and Fig. 3C_4 bottom left).

On the contrary, SEM image of CZ@C HT RM nanocomposite depicts a distinguished morphology with the appearance of leaf shaped particles (Fig. 3D_1 top left). This is an indication that the hydrothermal treatment

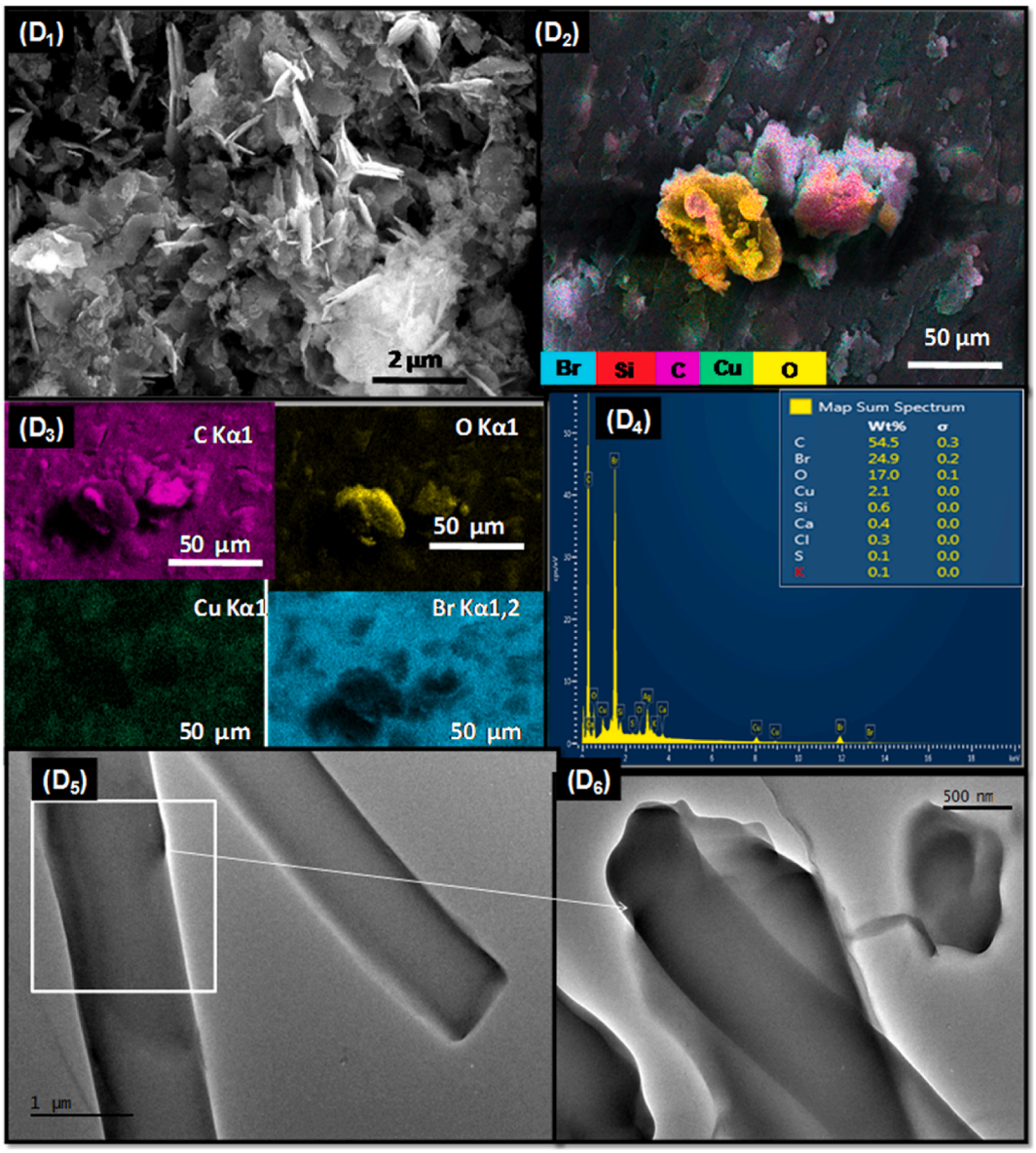

Fig. 3. (*continued*).

of the reversed micelle synthesis gel produces changes in the nanocrystallites aggregation forming lauric acid and organic-based compound shell, which coats a core composed of Cu e Zn particles. As a result, the core-shell structure is well crystallized under autogenous pressure due to the relatively high temperature of the hydrothermal treatment, in agreement with XRD results. Additionally, C, Cu, Br and O are visible on the solid surface, according to the EDS mapping (Fig. 3D_2 top right and Fig. 3D_3 center left). Although Cu is present in large amounts on the solid surface, Zn is not detected in the EDS spectrum (Fig. 3D_4 center right), but impurities such as Si are observed. Moreover, the TEM image of the CZ@C HT RM confirms that the leaves are well crystallized as nanorods (Fig. 3D_5 TEM micrograph, left bottom), which comprise the metal oxide nuclei involved in the carbon shell (the included Fig. 3D_6 TEM micrograph, bottom right). Also, voids are created between the nanocrystallites, having the latter an average diameter of 13 nm. It could be an indication of a hollow core-shell structure.

Importantly, all nanocomposites have a very low nitrogen adsorption capacity (Fig. S3). It is supposed that the debris of the carbonized organic precursors can be timely occluding the pores of the solids. Another possibility is that the residual carbon species along with the metal oxide into the core can also be on the surface, implying in the accumulation of these species and the consequent lack of porosity. This proves that the nanocomposites are comprised primarily of crystallized carbon species from lauric acid through the synthesis by the associated ultrasonic and reverse micelle methods.

3.3. Physicochemical properties of the CZA solids obtained from CZ@C HT RM nanocomposite

The CZ@C HT RM nanocomposite synthesis route is chosen to obtain a lauric acid chelated with a metal oxide phase in a core-shell structure. The XRD pattern of the as-synthesized CZA@C HT RM (Fig. 4A) illustrates that the introduction of aluminum during the synthesis of the nanocomposite does not alter the structural features of the solid, comparing with the CZ@C HT RM counterpart (Fig. 2A).

Accordingly, the XRD pattern of the CZA@C HT RM displays the diffused peaks of lauric acid in low 2θ regions. Also, four well resolved peaks of cubic CuO are visible at $2\theta = 34.1$, 36.2, 49.3 and 57.2°, which can be indexed to the (002), (100), (202) and (020) crystalline planes,

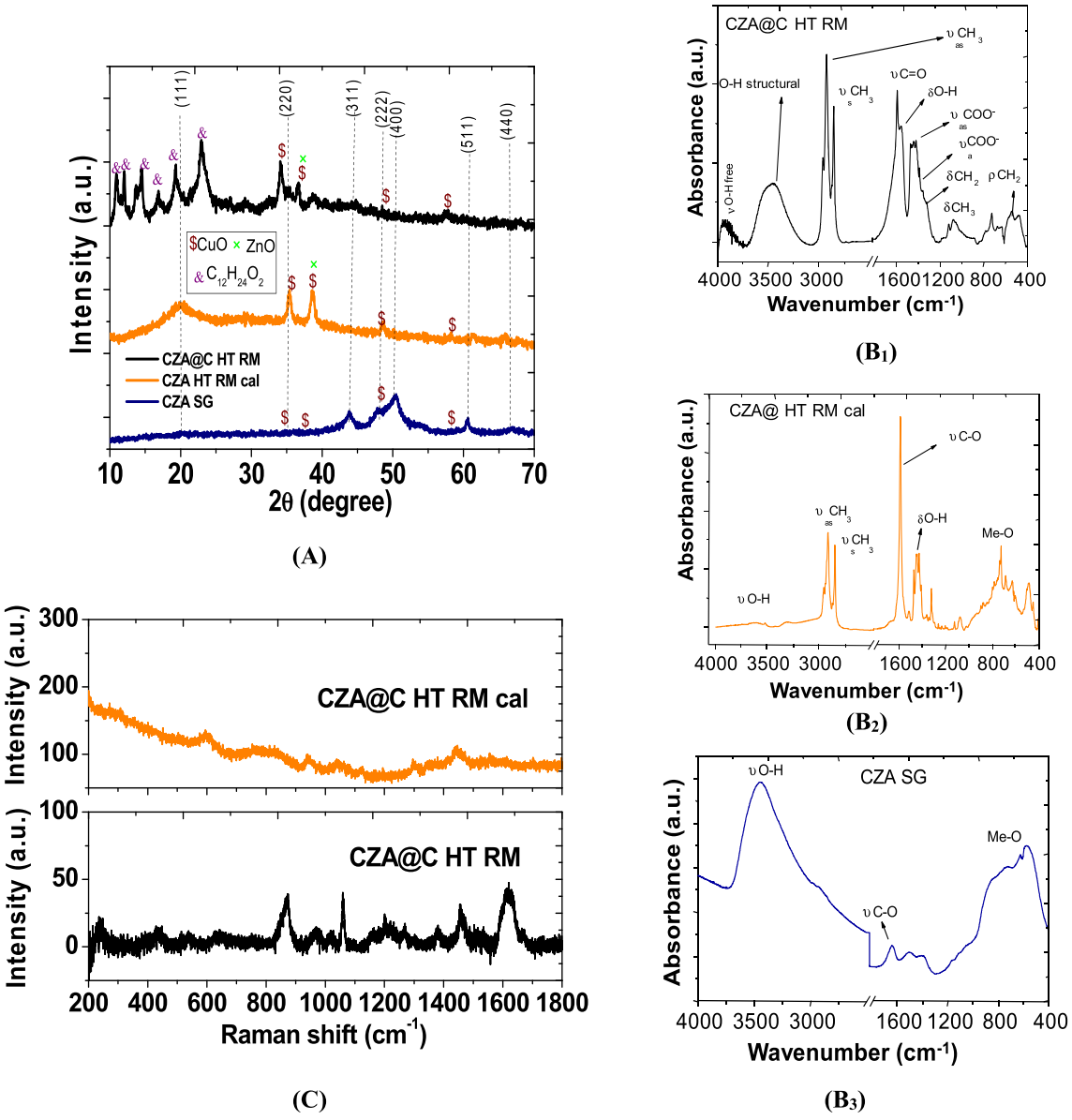

Fig. 4. Structural characterizations by (A) XRD patterns (B) FTIR and (C) Raman measurements of the CZA nanocomposites.

respectively. Although the XRD peaks of ZnO cannot be clearly detected under the detection sensitivity of the technique, the hexagonal ZnO phase is likely present in an amorphous state and/or with a relatively low amount into the nuclei. The previous visible cubic Cu_2O phase in the CZ@C HT RM analog has lower intensity due to the fact that its particle sizes are not enough to generate XRD peaks. It is important to note that the peaks appear in a similar position as those of the semicrystalline boehmite γ-AlOOH phase (JCPDS file 100425) thus, the presence of aluminum oxyhydroxide cannot be excluded in the CZA@C HT RM diffractogram. This indicates that aluminum readily promoted the interaction of the copper and zinc species present into the core with lauric acid and the organics shell without agglomeration of particles.

The synthetic route results in the regulation of the crystal growth during the sonochemical procedure allowing a good crystallization of the sample during the hydrothermal treatment. Finally, the aforesaid HT procedure generates the semicrystalline CZA@C HT RM nanocomposite (Fig. 4A). Our previous study on alumina-based catalysts synthesized without ultrasonic treatment has demonstrated the low crystallinity and the agglomeration of the metal nanoparticles on the support [15,19], being a disadvantage directly comparing with the sonochemical route.

Upon calcination of the CZA@C HT RM sample in an oxidant atmosphere, the lauric acid is vanished from the structure while the CZA@C HT RM cal sample shows the main diffraction peaks of semicrystalline cubic γ-Al_2O_3 at 19.9 (111), 33.0 (220), 44.1 (311), 44.2 (222), 50.0 (400), 61.6 (511), and 65.7° (440), in agreement with JCPDS 10–425. Besides, the peaks of highly dispersed of CuO in close contact with ZnO on the surface of γ-Al_2O_3 are observed in the CZA@C HT RM cal sample. In other words, the peaks attributed to lauric acid are vanished from the XRD diffractogram, instead, the cubic γ-Al_2O_3 peaks belonging to the *Fd3m* along with those of CuO and ZnO appear in the diffractogram. Some of the CuO peaks exhibited a small displacement to higher 2θ values in CZA@C HT RM cal as an effect of the diminution in lattice parameters owing to the strong interaction between CuO and γ-Al_2O_3 support. As the Cu_2O phase is not detected, it may be suggested that the reduction of the copper species does not take place due to the oxidation of lauric acid to CO or CO_2, which would promote the oxidative transformation of Cu_2O to the CuO phase.

The CZA SG sample prepared by sol-gel method exhibits the peaks of cubic γ-Al_2O_3. Moreover, small crystalline peaks of the CuO phase appear in the diffractogram, which indicates that the sol-gel method

gives highly dispersed CuO and ZnO oxides on the surface of γ-Al_2O_3. Because of the detect limitation, the peaks of ZnO are hardly observed among all peaks in the XRD patterns.

Fourier transform infrared spectra of the solids demonstrate that the absorption bands of the non-calcined precursor CZA@C HT RM nanocomposite (Fig. 4B_1) are mainly composed of carbonized lauric acid and other precursor, in similar fashion as those of the CZ@C HT RM analogue (Fig. S2). As a result, the absorption band at around 3360 cm^{-1} is due to either stretching vibration of structural Me–OH or OH groups from physisorbed water [30]. Also, the stretching vibration absorptive band of the deformation of OH is visible at 1660 cm^{-1}. Table 1 shows the attributions of the FTIR absorption bands of the solids.

In particular, the aliphatic region of the FTIR spectrum of CZA@C HT RM depicts bands at around 2948 and 2850 cm^{-1}, which are associated with the anti-symmetric $\nu_{as}(CH_2)$ and symmetric $\nu_s(CH_2)$ and C–H stretching vibrations of lauric acid [21,33]. Importantly, bands at around 1500 and 1300 cm^{-1} are associated with the CH_2 bending and CH_3 rocking modes of lauric acid, respectively. Moreover, the strong absorption band at about 1700 cm^{-1} is due to the CdO stretch dimer H-bonded of lauric acid [34]. However, the carboxylate group vibration originally at around 1700 cm^{-1} is shifted to lower frequencies regions e.g., 1590 cm^{-1}. This suggests a change in the vibrational features of the CZA@C HT RM due to the stretching carboxylate species *i.e.*, COO^- mode, which coordinates with metal cations through chelation. The minor bands are visible at 1060 and 1134 cm^{-1} ν_{as} (C–C) and ν_s (C–C) stretching appears, respectively. In addition, the broad absorption bands at high frequencies below 692 cm^{-1} for CZA@C HT RM are clearly visible due to the ρCH_2 vibrations, as discussed in the previous section.

FTIR curve of CZA@C HT RM cal (Fig. 4B_2) evidences a broad band basically similar to that of CZA@C HT RM (Fig. 4B_1) coming from physisorbed water molecules in the at 3200-3800 cm^{-1} region is vanished from the spectrum due to the calcination of the solid, as expected. Simultaneously, the intensity of the band at around 3340 cm^{-1} in CZA@C HT RM cal becomes less pronounced in comparison with that of CZ@C HT RM because the structural OH groups are prevalent, when the calcination of the former sample provides the elimination of water. Similar observations can be drawn for the band at 1620 cm^{-1} due to physisorbed OH groups [35]. Also, bands assigned to Al–O bonds from boehmite AlOOH can be detected below 900 cm^{-1}.

Notably, the bands of as C–H vibrations coming from the paraffinic chains of lauric acid are not completely vanished from the spectrum of the CZA@C HT RM cal sample, as result of the highly ordered residual lauric acid chain, which remains even after the calcination of the solid. This suggests that calcination of the CZA@C HT RM sample gives isolated CuO and ZnO phases, which are also embedded into the Al_2O_3 lattice and lauric acid chains.

The FTIR spectrum of CZA SG (Fig. 4B_3) exhibits similar features as those of CZA@C HT RM cal with a preeminent absorption band at around 3400 cm^{-1}, attributable to the OH groups from both alumina and physically adsorbed water, in good agreement with the XRD results. Noteworthy is the appearance of a band at 1620 cm^{-1} that can be assigned to the stretching vibrations of C–O bonds from CO_2. Below 600 cm^{-1}, the appearance of metal-O bands is evident in all solids. The overall FTIR measurement thus suggests that the CZA solids are semi-crystallines, in accordance with the XRD results.

The Raman spectra of the CZA@C HT RM and CZA@C HT RM cal are displayed in Fig. 4. Due to the strong luminescence of the aluminum compound, it is not possible to obtain the Raman spectrum of CZA SG in a similar fashion as Al_2O_3-based compounds [36].

For the CZA@C HT RM (Fig. 4C_1), the spectral region of 200–800 cm^{-1} shows broad bands at around 235, 448, 538, 641 and 753 cm^{-1}. These vibrational modes are ascribed to the combination of the paraffinic chain bending with the oxygen stretching mode of the H-bonded dimer and lattice vibration modes, as well [28,37].

The ill-defined vibrational modes around 855 and 976 cm^{-1} are mostly due to the doublets of $\rho(CH_2)$ rocking modes. Additionally, the modes observed at about 1020, 1058 and a triplet ranging between 1070 and 1299 cm^{-1} are attributed to νC-C stretching modes. The modes around 1381, 1460 and 1657 cm^{-1} are assigned to $\delta(CH_2)$ scissoring mode and CH_3 group vibrations [37].

As discussed before, studies on the lauric acid triclinic structure demonstrate that the single crystal structures have the A_1, A_2, A_3 and A_{super} forms. All of these forms have a carboxylic head connected to a zig-zag paraffinic chain, which is ended with a CH_3 group; both C and A dimmers are stabilized by a strong H-bond between two adjacent carboxylic heads [28]. Because of the similarity of the CZ@C HT RM nanocomposite spectrum positions and frequencies, it is likely that the triclinic structure of lauric acid is present in the spectrum of CZA@C HT RM. Importantly, the vibrational modes of lauric acid arise at similar positions to those of cubic Cu_2O and CuO and hexagonal ZnO, in good agreement with the XRD results.

Comparably, Raman spectra of CZA@C HT RM and CZA@C HT RM cal (Fig. 4C) depict substantial spectral changes. This is obviously correlated with their different structures.

Accordingly, most of the organic compound bands are vanished from the spectra essentially in reason of the calcination of the solid. Notably, vibrational modes at 584, 811,954, 1038, 1297 and 1447 cm^{-1} contribute with broad bands at the same position as those reported for the CuO and ZnO phases [29,30]. Furthermore, the bands at 1297 and 1447 cm^{-1} suggest the existence of residual hydrocarbon groups in the sample, after thermal treatment at 300 °C in an oxidant atmosphere, in agreement with the FTIR results.

3.4. Morphology and texture of CZA nanocomposites prepared by distinct methods

Fig. 5 shows the SEM micrographs of the CZA samples. The SEM image of the CZA@C HT RM sample (Fig. 5A_1) shows that aluminum introduction affects significantly the morphology of the solid, in comparison to the CZ@C HT RM analogue (Fig. 3D). The roof tiles stacked-like morphology illustrates that the rod consisted mostly of aggregated crystalline particles with a rough surface (Fig. 5A_1, top left). This presumably shows the successful insertion of Al into the core that contains already the CuO and ZnO oxides coating the semicrystalline layer that is formed by carbon in the outer shell.

The EDS mapping (Fig. 5A_2, top right) clearly exhibits the presence of Cu, Al, and O, while Zn is not detected on the solid surface the CZA@C HT RM sample. In addition, the hydrothermal treatment significantly distributes Cu and Al in a uniform fashion throughout the solid surface, as can be seen in the EDS mapping (Fig. 5A_3, center left). Because the vast amount of carbon on the surface of ca. 73.6 wt% is mainly coming from lauric acid and other organics, Zn is not detected specifically in the region evaluated whereas Cu and Al elements are in minor amounts (Fig. 5A_4, center right).

This corroborates with the XRD results that show the semi-crystalline acid lauric structure as a major phase present in the solid. Regarding the low magnification TEM image, it is possible to observe some isolated nuclei in the form of spheres (Fig. 5A_5, bottom left), which contain a dense core consisting of Al, Cu and Zn species (Fig. 5A_5, bottom left inset). A magnified view of the TEM image (Fig. 5A_6, bottom right) confirms that the dark nuclei are dense arising from the metallic species, whereas a lighter shell is composed of lauric acid and other organics, which is coating the nuclei with metal oxide nanoparticles. Apart from the dominant amount of isolated sphere shaped nuclei, the HRTEM images (Fig. 5A_6, bottom right inset) suggest that these nuclei are poorly crystalline with a lighter shell region possessing thickness or diameter constrained to tens of nanometers. Thus, the carboxylated fatty acid may interact with the metals, allowing the assumption that Cu and Zn may be embedded into the isolated Al_2O_3 lattice and the combination of the reverse micelle and sonication steps accompanied by the hydrothermal method have effectively avoided the clustering of the particles.

Through calcination of CZ@C HT RM, the sample undergoes a jelly

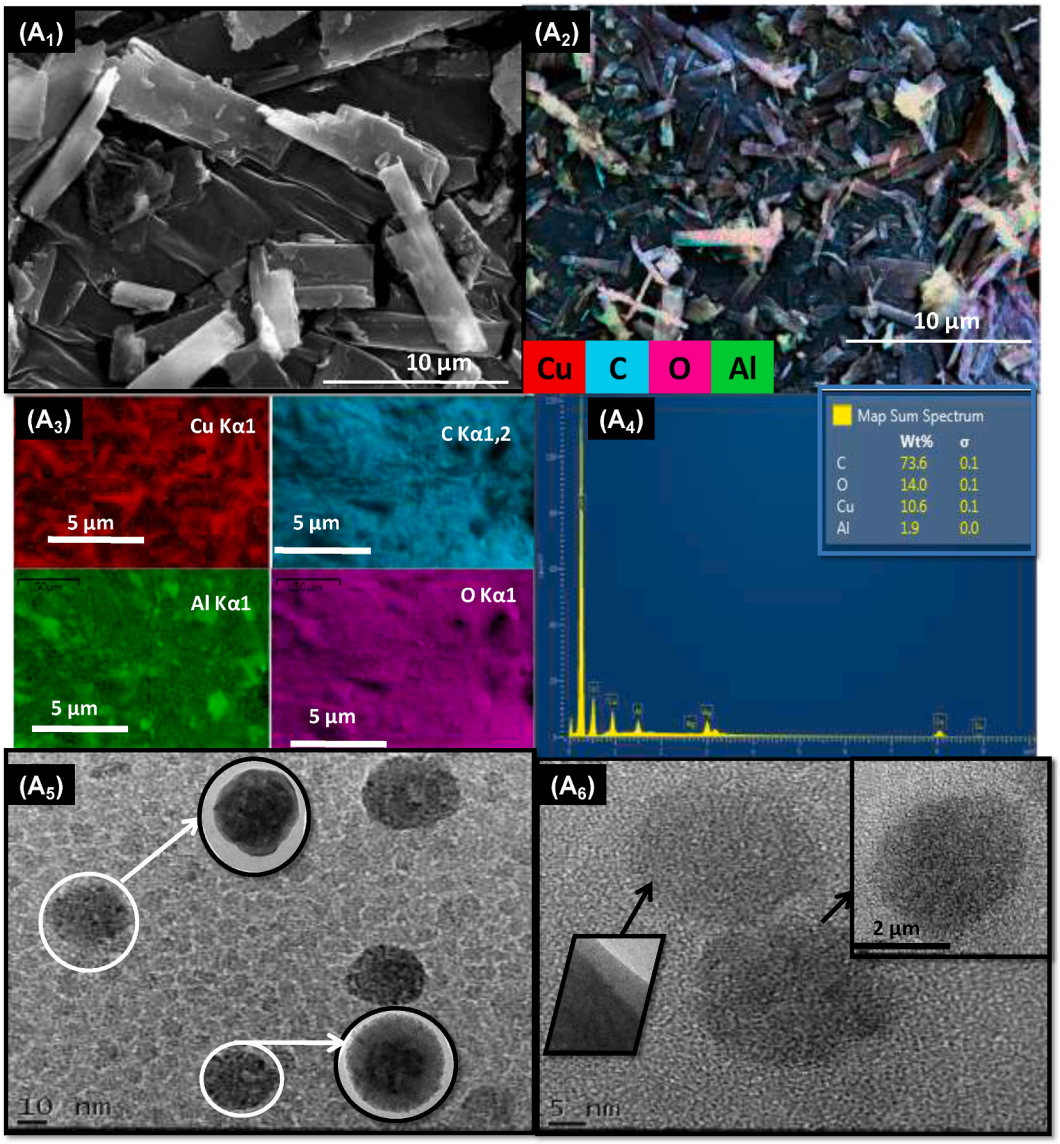

Fig. 5. SEM micrographs, EDS images mapping and spectra of the CZA solids: (A) CZA@C HT RM and (B) CZA@C HT RM cal. The TEM image of CZA@C HT RM and CZA@C HT RM cal are in the bottom of the figure. Inset: corresponding HRTEM images of CZA@C HT RM.

fish tentacles shaped morphology (Fig. 5B_1, top left). The magnified image of CZA@C HT RM cal suggests that a self-assembled of the jelly fish tentacles like particle surface is smooth (Fig. 5B_2, SEM image bottom left) with Cu, Al and Zn migrating to the solid surface (Fig. 5B_3, EDS mapping top right and Fig. 5B_4, TEM image bottom left). From the composition according to the EDS spectrum (Fig. 5B_5, center right), it appears that the shell could consist of 79.5, 15.5 and 1.0 wt% for Cu, Zn and Al, respectively. Residual carbon is seen in low amounts, in agreement with Raman and FTIR spectra. This could suggest that removal of the shell through calcination may result in a nanostructured solid. During the synthesis, the lauric acid, PVP and CTAB soft templating would promote a surface reaction between the carbonyl, hydroxyl and amino groups with the metallic species present into the core. After the removal of the outer part of the shell, the formation of a nanostructure is likely, as found elsewhere [35]. Another point is that the γ-Al_2O_3 phase (XRD results) is formed from aluminum hydroxide and boehmite oxyhydroxide precursors, which are converted to the transition alumina phase (Fig. 5B_6, bottom right TEM image), upon heating in air treatment. Thus, it is possible that CuO and ZnO are dispersed on the alumina surface through calcination (Fig. 5B_6, TEM image bottom left).

On the other hand, the SEM image of CZA SG (not shown) depicts aggregation of the small nanorods particles, as found for ZnO based synthesized via sol-gel method [15,19]. This indicates that that the sol-gel method results in the dispersion of CuO and ZnO nanoparticles on Al_2O_3 followed by calcination of the sample, causing the formation of particles, most of them agglomerated.

Fig. 6 shows the physisorption isotherms of the CZA composites. As it can be seen, the adsorption and desorption branches of the CZA@C HT RM isotherm (Fig. S3) do not fit, which is possibly due to the synthesis debris on solid surface and complete pore filling with metallic nanoparticles, as well. In comparison with CZ@C counterparts, the CZA@C HT RM is a porous solid and its low textural properties are probably due to the aluminum role as spacer into the solid structure.

Besides that, the debris also contributes to the low surface area and pore volume of the sample, even if the carbon shell is porous (Table 2).

The type IV isotherm with H_3 hysteresis loop is shown for CZA@C HT RM cal (Fig. 6A_1), which demonstrates the porosity of the solid, after the removal of part of the organics. The steep augmentation and high adsorption at $P/P_o > 0.9$ suggests the presence of irregular pores and a very low interparticle porosity [39]. As calcination causes crystal

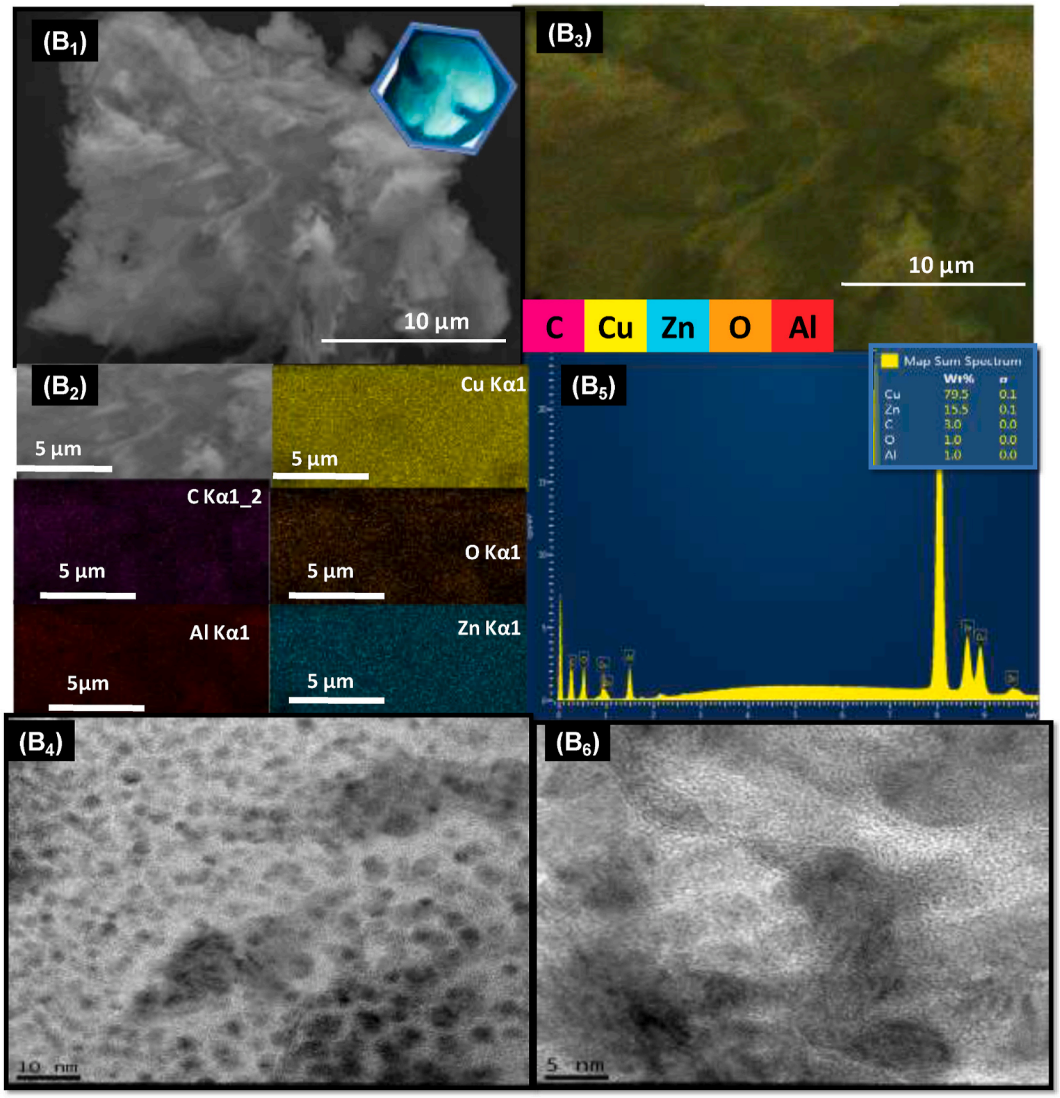

Fig. 5. (*continued*).

aggregation in some extent, the occurrence of single, twin, triple or multiple core particles coexisting in the materials may be possible.

On the contrary, CZA SG gives a type IV isotherm with a hysteresis loop between H_2 and H_3 (Fig. 6A_2). Further, the sharp capillary condensation steps take place at the region of $P/P_o = 0.5$ evidencing the presence of pores with diameters larger than micropores [23,38]. It is showing good agreement with the XRD and nitrogen physisorption results that show CuO and ZnO mostly dispersed on an Al_2O_3 support.

The textural properties of the solids are summarized in Table 2. As expected, the synthesis debris contributes to the low BET surface area and pore volume of CZA@C HT RM with microporosity arising from the carbon shell, as demonstrated by the *t*-plot surface area. Obviously, CZA@C HT RM cal displays a 10-fold higher BET surface area and pore volume than the CZA@C HT RM counterpart due to the elimination of part of the organics upon calcination. Accordingly, CZA@C HT RM cal has high surface areas (30 $m^2\ g^{-1}$) and bigger pore volumes (0.10 $cm^3\ g^{-1}$), when comparing the same parameters for CZA@C HT RM. Also, numerous micropores are created upon calcinating the solid in reason of carbon burnt that forms CO_2 leaving from the solid and letting behind the micropores, as demonstrated by the high *t*-plot area.

Compared to CZA@C HT RM cal, CZA SG holds a remarkable surface areas and pores volumes among the CZA solids studied thanks to the good dispersion of CuO and ZnO oxides on alumina. For instance, the BET surface area is ca. 60 $m^2\ g^{-1}$ and the mesopore volume value is 0.19 $cm^3\ g^{-1}$, as expected for the sol-gel based samples. The micropores surface areas are amongst the most studied because of the complete removal of the carbon sources, leaving the micropores behind in the solid, as expected.

The pore diameter curves exhibit a non-uniform distribution of the pores for CZA@C HT RM cal (Fig. 6B_1), but this last solid preserves the typical mesoporous structure. Similar features extend to the pore diameters with CZA SG (Fig. 6B_2), having a pore diameter around 4.8 nm, slightly larger than that of CZA@C HT RM cal. Contrary, the pore diameter of CZA@C HT RM is ca. 2.7 nm indicating that there is no collapse of the mesopores structure caused by excess synthesis debris, which could be deposited on the solid surface but is not present inside the mesopores.

3.5. XPS analyses of the CZA solids

X-ray photoelectron spectroscopy (XPS) analyses are carried out to further determine the valence states of the elements and their surface chemical compositions for the CZA samples.

The Zn *2p*, O *1s*, C *1s* and Cu *2p* core levels spectra are observed for the CZ@C HT RM nanocomposite precursor. The binding energy values for Zn $2p_{3/2}$ and O *1s* core levels are 1022.0 and 531.8 eV, respectively

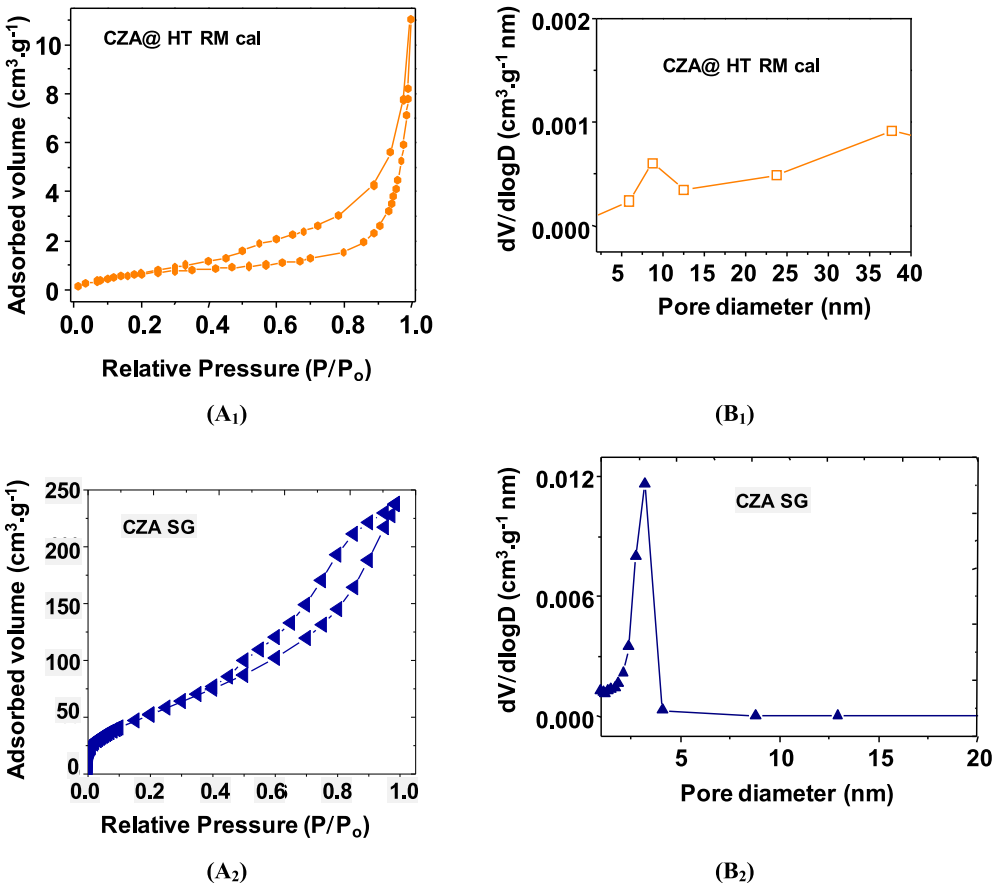

Fig. 6. (A) Nitrogen adsorption-desorption isotherms and (B) pore size distribution curves of the CZA solids.

Table 2
Textural properties of the CZA solids in study.

Sample	Sg_{BET} (m^2 g^{-1})	Sg t-plot (m^2 g^{-1})	V_P (cm^3 g^{-1})	[b] Pore size (nm)
CZA@C HT RM	3	4	0.01	2.7
CZA@C HT RM cal	30	38	0.10	4.8
CZA SG	57	62	0.19	4.7

[a]BET surface area.
[b] BJH method desorption branch of the isotherms.

(Table 3). This indicates the existence of Zn^{2+} coming from ZnO on the solid surface, as found elsewhere [40]. Noteworthy, multi-peaks of kinetic energy Auger Zn LMM are visible with the major contribution at about 500.3 eV. This would suggest the lower electron density of Zn^{x+} species as found for the Al^{3+}-containing CZA samples [41].

Three contributions for C *1s* core levels appear at 284.8, 286.1 and 288.7 eV. The most intense peak centered at 284.8 eV representing 88% of the contribution is the same position as that exhibited by C═C/CH bonds [40,41]. Importantly, adventitious carbon species is present with binding energy value of 284.8 eV and thus, its occurrence cannot be ruled out [42]. The weaker contribution at higher binding energy e.g., 286.1 (60%) is ascribed to C–OH and C–N bonds [40]. At 288.7 eV, the component contributes with 6% of the total area of the peak being associated with COO^- species [20,40]. In the case of the O *1s* core level spectrum, the binding energy at 531.8 eV is assigned to the major abundance of chemisorbed oxygen species on the solid surface arising

Table 3
Binding energy values from XPS spectra of the nanocomposites and percentage of the species present in the solids.

Sample	Binding Energy (eV)					
	C *1s*	O *1s*	Cu $2p_{3/2}$	Zn $2p_{3/2}$	N 1*s*	Al 2*p*
CZ@C HT RM	284.8 (88%) 286.1 (6%) 288.7 (6%)	531.8	932.3	1022.0	–	–
CZA@C HT RM	284.8 (81%) 286.1 (17%) 288. 6 (2%)	532.2	932.6 (62%) 935.0 (38%)	1022.1	402.3	74.1
CZA SG	284.5 (86%) 285.7 (8%) 288.9 (6%)	530.8	932.6 (56%) 934.3 (44%)	1021.7	–	73.9
CZA@C HT RM cal	284.8 (76%) 286.1 (17%) 288.9 (7%)	531.1	933.1 (58%) 934.9 (42%)	1021.9		74.1

from Oα, O_2^{2-}, O^-, OH^- or CO_3^{2-} [40]. Besides, the possibility of the C–O bond at 531.8 eV is excluded. Owing to lauric acid, PVP, CTAB and PEG compounds that formed the shell, these oxygen species, especially lattice oxygen from the surface of the nanocomposite, are inevitably formed. These results certify the formation of lauric acid in the shell in good agreement with the XRD, TEM, Raman and FTIR results.

The Cu 2*p* core level spectra are shown in Fig. 7. The CZ@C HT RM nanocomposite depicts the doublet Cu $2p_{3/2}$ - Cu $2p_{1/2}$ (Fig. 7a). Of importance, both Cu $2p_{3/2}$ and Cu LMM Auger peaks are seldom used to determine the oxidation states of copper species [43]. The Cu $2p_{3/2}$ core level shows an intense peak at 932.2 eV, typical of reduced Cu species, mainly Cu^+. The contribution of Cu $2p_{3/2}$ core level is seen through a very weak shake up satellite at 932.5 eV. This indicates the existence of Cu^{2+} on the surface [40]. These results are in line with the XRD data that show copper existing as CuO and Cu_2O phases. Besides, the relative surface content of Cu^{2+}/Cu^+ ions are calculated from the integrated areas of Cu $2p_{3/2}$ core level contributions, which are derived from the raw XPS data. It is observed an increase in the Cu^{2+}/Cu^+ values, indicative of an enrichment of Cu^{2+} ions on the solid surface but it can be accounted to the Cu species migrating from the nuclei. It can be read as the coverage of Cu species by lauric acid shell or Al or Zn oxides interaction with Cu in the core.

Interestingly, the atomic percentages on the surface reveal the following amounts for C, O, Cu and Zn of 85.88, 10.35, 0.44 and 3.33%, respectively. From these values, the C/Cu atomic surface ratio is 195 for the CZ@C HT RM nanocomposite. Considering that this value is higher than that of the nominal one (134), it could indicate that the Cu atoms are enriched on even the C atoms arising from lauric acid structure have defects on surface.

For the CZA@C HT RM sample, the Zn *2p*, and C *1s* binding energies values remain practically unchanged evidencing the same species are present in the core-shell structure. Besides, the N *1s* core level spectrum appears at 402.3 eV comfortably lying close to the value suggested for C *1s* core level at 286.1 eV identified as a protonated amine bond. On the other hand, in the case of CZA@C HT RM (Fig. 7b), two contributions are observed in the Cu $2p_{3/2}$ spectrum at 932.6 eV (62%) and 935.0 eV (38%) being assigned to Cu^+ and Cu^{2+} species. This confirms that Cu^+ from Cu_2O ions may be transformed into Cu^{2+} upon addition of aluminum in the nanocomposite, in agreement with the XRD data. Also, the appearance of the satellite peaks at 940.9 and 943.7 eV suggests the presence of the CuO phase. Furthermore, the Al *2p* core level spectrum appears with a binding energy of 74.1 eV in good consistence with the expected Al^{3+} ion [15], which arises from γ-AlOOH phase. Additionally, the O *1s* core level shifts toward higher binding energies value of 532.2 eV, which ascertains the presence of γ-AlOOH.

In addition, the atomic concentrations on surface for C, O, Cu, N and Zn are 87.47, 7.72, 0.46, 2.45 and 0.80%, respectively. A slight change is observed for the C/Cu atomic surface ratio (190), indicating a slight Cu migration to the surface. This behavior can be explained by taking into consideration that the aluminum atoms are into the nuclei and also exposed on surface and attached to the carbon by C–O–Al bonding, whose origin occurred during the synthesis processes. As demonstrated by EDS results of CZA@C HT RM, Cu is found in high amounts on solid surface.

The CZA@C HT RM cal sample presents the binding energies for Al *2p*, O *1s* and C *1s* core level unchanged. Interestingly, the *Zn* $2p_{3/2}$ peak appears implying the maintenance of Al^{3+} ion and C species observed for the CZA@C HT RM analogue. Moreover, a doublet peaks attributed to Zn $2p_{3/2}$ and Zn $2p_{1/2}$ at 1021.9 and 1045.0 eV that are similar to those found for the standard reference of ZnO [40]. The calcined sample CZA@ HT RM cal shows a Cu $2p_{3/2}$ spectrum with two contributions (Fig. 7c), but the contribution at low binding energy appears at 933.1 eV (58%) and this value cannot be assigned to Cu^+. This value is typical of Cu^{2+} species with a strong interaction with the support. This supports the assumption that Cu^+ could be oxidized upon calcination in air resulting in the environment of Cu^{2+} at the top surface strongly interacting with Zn^{2+} and Al^{3+} species. It could suggest the good dispersion of Zn and Cu oxides species on alumina surface. The Cu $2p_{3/2}$ core level

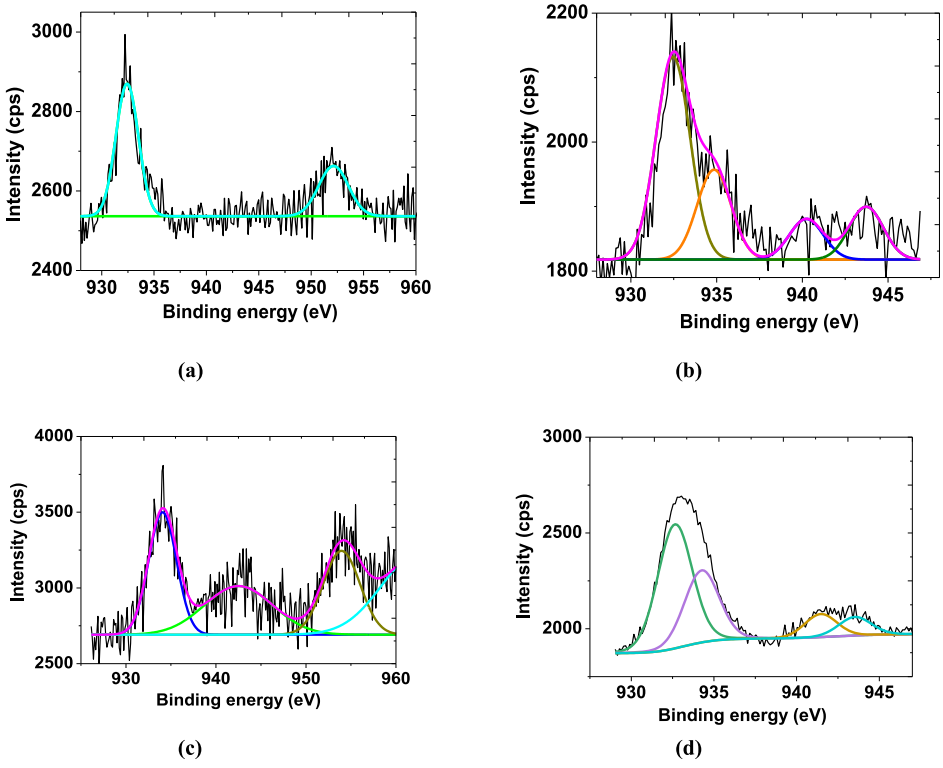

Fig. 7. Cu *2p* region obtained from XPS analysis of the solids: (a) CZ@C HT RM, (b) CZA@C HT RM, (c) CZA@C HT RM cal and (d) CZA SG.

spectrum of sample CZA SG also shows two contributions at 932.7 eV (57%) and 934.8 eV (43%) assigned to Cu^{+} and Cu^{2+}, but now the proportion of Cu^{2+} increases.

Besides, it is remarkable that the atomic concentration percentages are 15.72, 56.68, 22.71, 1.21 and 3.68% for C, O, Al, Cu and Zn, respectively. As expected, the calcination provokes the removal of almost all carbon, the huge increase of the O and Al contents, and the higher observed contents of Cu and Zn.

The CZA SG sample (Fig. 7d) has similar XPS features of that of CZA@C HT RM cal (Fig. 7a), in terms of Cu^{2+}, Zn^{2+} and Al^{3+} species but concentrations of the Cu and Zn ones on surface are lower than those of CZA@C HT RM cal. It could be ascribed to the better dispersion of the nanoparticles on the latter sample due to the combined-sonochemical core/shell synthesis assisted by reverse micellization route.

3.6. Ethylbenzene oxidation reaction in the presence of hydrogen peroxide

The catalytic evaluation of solids is investigated in the ethylbenzene oxidation reaction in the presence of hydrogen peroxide (Fig. 1). This reaction is particularly interesting since the acetophenone, benzoic acid and benzaldehyde products are used in perfumery, cosmetics and as intermediates for the synthesis of valuable compounds [9,44].

Blank runs evidenced that hydrogen peroxide alone is not suitable to oxidize ethylbenzene in the absence of the catalysts. The CuO nanoparticles are found to have an EB conversion of 5% after 3 h of reaction but, the activity is negligible within 6 h due to the lack of Cu species stability in the reaction media. Since Cu^{2+} species are responsible for the activity in the EB oxidation reactions [17,45], it is expected that all CZ@C and CZA@C nanocomposites as well as the reference CZA solids would be active.

Fig. 8 summarizes the EB conversion over the studied solids. Significant difference of EB conversion performances can be observed, when CZA solids and CZA@C are compared to the CZ@C nanocomposites (Fig. 8a). The latter solids have a poor performance *e.g.*, less than 7% of EB conversion within 6 h of reaction that is attributed to the Cu species leaching during the reaction. Accordingly, the bluish color of the reaction solutions evidences the Cu leaching after filtration of the catalyst.

Meanwhile, the worst EB conversions are achieved for CZ@C R RM, CZ@C RR RM and CZ@C RA RM, which is indeed less than half of the performance for CZ@C HT RM. It is more clearly found that EB conversion accounts for less than 3% in the case of CZ@C R RM, CZ@C RR RM and CZ@C RA RM samples. Besides, the EB conversion reaches 7% over CZ@C HT RM, being slightly higher than that of CZ@C RA RM under the same conditions tested. Most probably, Cu^{2+}/Cu^{+} and Zn^{2+} ions present into the CZ@C nanocomposite cores make a suitable condition as active sites for EB transformation in the presence of H_2O_2 as oxidant. However, the accessibility of reactants throughout the low ordered lauric acid structure that mainly involves aggregate of platelets or large bulky rod aggregates is restrained. Hence, a reliable assessment of EB and H_2O_2 to diffuse in a non-porous carbon shell to reach the copper domains into the cores does not occur efficiently. Indeed, homogeneous catalysis takes place due to the leaching of the Cu active center of the as-synthesized CZ@C nanocomposites, which are less actives than the other solids studied.

Overall, CZA@C and CZA display superior performances in comparison with the CZ@C solids. For instance, the EB conversion over CZA@C HT RM is of ca 12%, which is appreciably good comparing with the corresponding as-synthesized CZ@C HT RM nanocomposite, which is marginally lower. Additionally, solid leaching losses of Cu are about 0.5 wt% of the total copper amount, which indicates that CZA@C HT RM nuclei have stability during EB oxidation. These observations suggest that the strong interaction between Cu^{2+}/Cu^{+} active species, Al^{3+} and Zn^{2+} coated by the lauric acid structure allow the oxidation reaction to occur in the core with no significant role played by either the lauric acid structure or free Cu species. Also, the performance of CZA@C HT RM also indicates that its crystallization takes part in the improvement of the activity of Cu species. When the lauric acid structure on the shell is exposed to the EB and H_2O_2, these reactants diffuse through the porous carbon shell and encounters Cu_2O, CuO and ZnO nanoparticles into the nuclei of CZA@C HT RM nanocomposite. As the carbon structure is not porous, the diffusion of the reactants to the nuclei is not easy and hydrogen peroxide may act by oxidizing the Cu sites on the surface of a part of the core, which promotes electron transfer with Al^{3+} and Zn^{2+}species.

The best performance of EB conversions is achieved over CZA solids. It is noteworthy that a remarkable catalytic activity of the CZA@C HT RM cal is demonstrated in comparison with the CZA@C HT RM and the reference CZA SG, which is very small. It could be indicating the diffusion of the reactants in CZA@C HT RM cal is through the porous alumina and carbon support. As CuO and ZnO nanoparticles strongly interact with the alumina support, an impressive 20% EB conversion is obtained. Also, the absence of metal ions in solution suggests that no leaching of Cu species takes place during the reaction and that they are present either on surface or intact into the pores.

The CZA SG solid possesses similar features as the CZA@C HT RM cal, but the CuO and ZnO supported alumina in the former solid exhibits EB conversion of only 14%, even though the Cu species are present in a large surface area. It is very likely that the formation of leached Cu^{2+} in solution makes CZA SG considerably less active than CZA@C HT RM cal solid, allowing the reaction to continue in the absence of any solid.

The selectivities to the reaction products are shown in Fig. 8b. It is important to note that the selectivity to acetophenone over the CZ@C HT RM nanocomposite is lower than 15% with slightly higher amounts

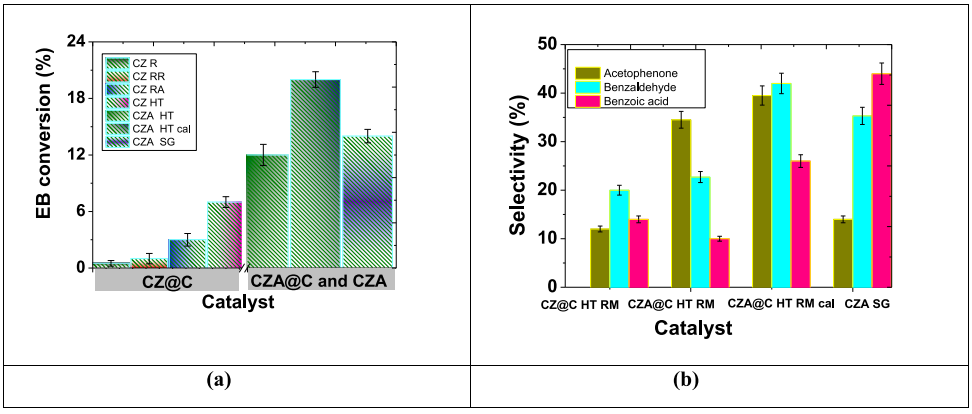

Fig. 8. (a) Catalytic evaluation of the solids in EB oxidation in the presence of H_2O_2 over all solids studied. (b) Selectivity to acetophenone, benzaldehyde and benzoic acid reaction products. Reaction conditions: 1 mmol ethylbenzene, 1 mmol H_2O_2, 50 mg catalyst at 50 °C for 6 h using acetone as solvent.

of benzaldehyde and benzoic acid obtained.

In the case of the CZ@C HT RM, CZ@C HT RM cal and CZA solids, the selectivities to acetophenone reach values of 34.7 and 39.3% for CZA@C HT RM and CZA@C HT cal, respectively (Fig. 8b). The significant difference in terms of properties of the CZA@C HT RM and CZA@C HT RM cal reveals that their catalytic properties are clearly dependent of the role of the aluminum presence into the core. As the Cu^{2+}/Cu^{+} species into the core of CZA@C HT RM will lose their electron to form the highest oxidation Metal-alkyl aromatic complex states in comparison with Zn^{2+}, the crucial role of the aluminum into the core is that of stabilizing the aforesaid complex to provide acetophenone formation. This is also valid for CZA@C HT RM cal, in which ZnO and CuO species are dispersed on alumina giving high conversion of ethylbenzene and the selectivity of acetophenone increased to some extent, suggesting that surface alumina as support has advantages for the liquid-phase selective oxidation of EB with H_2O_2.

A schematic representation of the EB oxidation reaction mechanism in the presence of hydrogen peroxide is tentatively proposed (Fig. 9).

First, H_2O_2 gets adsorbed on the electron deficient Cu^{2+} or Cu^{+} active sites on CZA@C HT RM cal catalyst to activate the oxygen–oxygen bonds of hydrogen peroxide and form hydroxyl radicals (Fig. 9, scheme I). These radicals are responsible for the formation of the alkyl radical highly oxidized Cu complex via a radical reaction mechanism [44,46]. Subsequently, the ȮH radicals act as electrophiles by activating the most reactive α-C-atom of the phenyl group of EB i.e., $–CH_2CH_3$ resulting in a homolytic cleavage of the C–H bond to form a benzyl intermediate

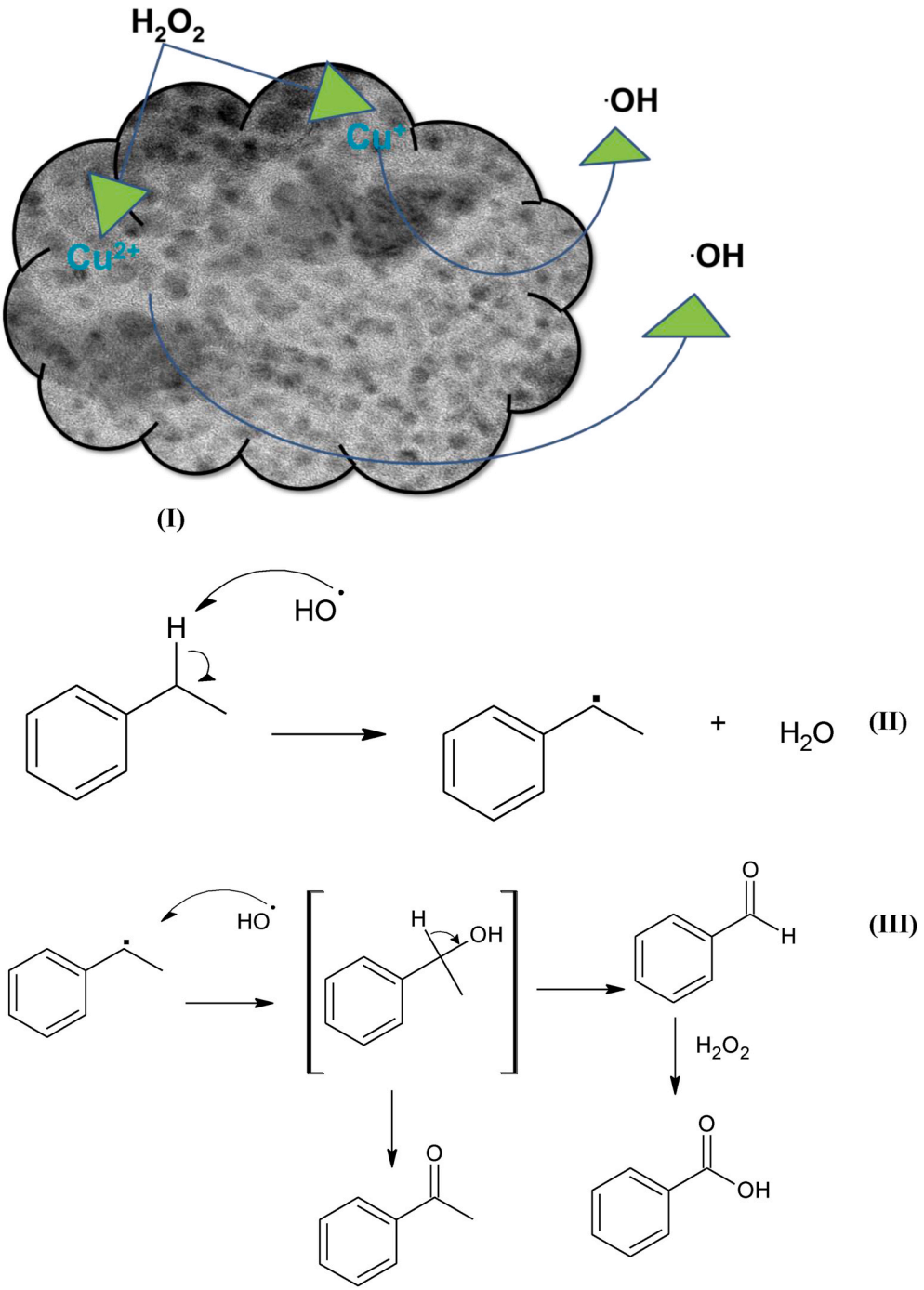

Fig. 9. Schematic representation of the mechanism for EB oxidation in the presence of H_2O_2 over the Cu active sites.

(Fig. 9, scheme II). Meanwhile, the excess ȮH radicals hydroxyl radical provides the capture of the hydrogen of the benzyl intermediate radical, which undergoes rearrangement to further form 1-phenylethyl hydroperoxide and ethylbenzene oxygen radical, as well [9,46]. Concomitantly, these intermediates may form acetophenone (Fig. 9, scheme III). Further oxidations on highly exposed Cu species allow benzaldehyde to be more easily oxidized to benzoic acid. (Fig. 9, scheme III). The last step might be the possible reason for the high selectivity to benzaldehyde over CZA@C HT RM cal and CZA SG due to the intimate contact of the Cu^{2+}/Cu^{+} species with Zn^{2+}.

More importantly, the best catalytic performance of CZA@C HT RM cal at such a high selectivity to the products suggests its great potential for EB oxidation reaction, when compared to the benchmark Fe-based catalysts used in the title reaction [9,45,46].

4. Conclusions

The CuZnAl@C core-shell nanocomposites had a stable structure containing Al, Zn and Cu oxide nanoparticles into a core with porous lauric acid acting as a shell. The porosity was significantly improved upon calcination of the CuZnAl@C nanocomposite to remove the lauric acid shell, resulting in the nanostructured CuO–ZnO/Al_2O_3 supported catalyst. The catalytic activity of the solid in EB oxidation in the presence of hydrogen peroxide was compared to a benchmark CuO–ZnO/Al_2O_3 supported catalyst obtained by the sol-gel method. In general, the best performances towards acetophenone, benzoic acid and benzaldehyde were attributed to the stability of Cu(II) and Al(III) species on alumina using distinct reaction conditions.

CRediT authorship contribution statement

José Vitor C. do Carmo: Conceptualization, Data curation, Formal analysis, Investigation, Methodology. **Rita de Cássia F. Bezerra:** Investigation, Methodology. **Samuel Tehuacanero-Cuapa:** Investigation, Methodology. **E. Rodríguez-Aguado:** Data curation, Formal analysis, Investigation, Methodology, Writing – review & editing. **Rossano Lang:** Methodology. **Adriana F. Campos:** Investigation, Methodology, Visualization. **Gian Duarte:** Investigation, Methodology. **Gilberto D. Saraiva:** Formal analysis, Funding acquisition, Investigation, Methodology, Writing – original draft. **Larissa Otubo:** Methodology. **Alcineia C. Oliveira:** Conceptualization, Formal analysis, Funding acquisition, Investigation, Visualization, Writing – original draft, Writing – review & editing. **E. Rodríguez-Castellón:** Formal analysis, Funding acquisition, Visualization, Writing – review & editing.

Declaration of competing interest

The authors declare that they have no known competing financial interests or personal relationships that could have appeared to influence the work reported in this paper.

Data availability

Data will be made available on request.

Acknowledgment

The authors thank Central Analítica da Universidade Federal do Ceará facilities used.This work was supported by the CNPq (406629/2018-8) and Funcap (PS1-0186-00346.01.00/21). E.R.C. and E.R.A. thank to Consejería de Transformación Económica, Industria, Conocimiento y Universidades (Project P20_00375) and Project PID2021-126235OB-C32 of Ministerio de Ciencia e Innovación (Spain) and FEDER funds. We also thank Dr. A Rodríguez-Gómez and Ing. S. Tehuacanero-Núñez from LCM-IFUNAM for granting access to the HRTEM. J.V.C acknowledges the scholarship from the Petrobras.

Appendix A. Supplementary data

Supplementary data to this article can be found online at https://doi.org/10.1016/j.matchemphys.2022.126800.

References

[1] P. Babaei, J. Safaei-Ghomi, l-proline covered N doped graphene quantum dots modified CuO/ZnO hexagonal nanocomposite as a robust retrievable catalyst in synthesis of substituted chiral 2-amino-4H-chromenes, Mater. Chem. Phys. 267 (2021), 124668.
[2] S. Sanati, Z. Rezvani, R. Abazari, Z. Hou, H. Daí, Hierarchical CuAl-layered double hydroxide/CoWO4 nanocomposites with enhanced efficiency for use in supercapacitors with long cycling stability, New J. Chem. 43 (2019) 15240–15248.
[3] A.A. Ali, E.A. El Fadaly, N.M. Deraz, Auto-combustion fabrication, structural, morphological and photocatalytic activity of CuO/ZnO/MgO nanocomposites, Mater. Chem. Phys. 270 (2021), 124762.
[4] A. Akhtar, C. Jiao, X. Chu, S. Liang, Y. Dong, L. He, Acetone sensing properties of the g–C_3N_4–CuO nanocomposites prepared by hydrothermal method, Mater. Chem. Phys. 265 (2021), 124375.
[5] J. Büker, X. Huang, J. Bitzer, W. Kleist, M. Muhler, B. Peng, Synthesis of Cu single atoms supported on mesoporous graphitic carbon nitride and their application in liquid-phase Aerobic oxidation of cyclohexene, ACS Catal. 11 (2021) 7863–7875.
[6] N.T. Dat, T.T.N. Mai, K.-S. Lin, N.T.M. Thu, N.T. Thao, Reactivity of styrene with tert-butyl hydroperoxide over Cu-based double hydroxide catalysts, Mol. Catal. 500 (2021), 111337.
[7] M. Behrens, I. Kasatkin, S. Kühl, G. Weinber, Phase-pure Cu,Zn,Al hydrotalcite-like materials as precursors for copper rich Cu/ZnO/Al_2O_3 catalysts, Chem. Mater. 2 (2010) 386–397.
[8] J. Kirar, S. Khare, Cu(II) Schiff base complex intercalated into layered double hydroxide for selective oxidation of ethylbenzene under solvent-free conditions, RSC Adv. 8 (2018) 18814–18827.
[9] J.V.C. Carmo, A.L.G. Pinheiro, A.C. Oliveira, M.O. de Castro, J.M. Soares, E. Padron-Hernandez, R. Peña-Garcia, G.D. Saraiva, E. Rodríguez-Castellón, E. Rodríguez-Aguado, Comparison of the catalytic performance of YIG garnets and Fe-containing oxides catalysts for oxidation of ethylbenzene, Ceram. Int. 47 (2021) 6279–6289.
[10] X. Dai, X. Li, S. Tang, X. Penga, X. Zheng, O. Jiang, Efficient aerobic oxidation of ethylbenzene accelerated by Cu species in hydrotalcites, Catal. Commun. 149 (2021), 10618.
[11] J. Schittkowski, H. Ruland, D. Laudenschleger, K. Girod, K. Kahler, S. Kaluza, M. Muhler, R. Schlogl, Methanol synthesis from steel mill exhaust gases: challenges for the industrial Cu/ZnO/Al_2O_3 catalyst, Chem. Ing. Tech. 10 (2018) 1419–1429.
[12] M. Sadeghini, M. Rezaei, A. Nemati, K. Maji, N. Jorabchi, B. Nematollahi, F. Zareiekordshoul, Effect of In_2O_3 on the structural properties and catalytic performance of the CuO/ZnO/Al_2O_3 catalyst in CO_2 and CO hydrogenation to methanol, Mol. Catal. 484 (2020), 110776.
[13] F. Zhang, X. Xu, Z. Qiu, B. Feng, Y. Liu, A. Xing, M. Fan, Improved Methanol Synthesis Performance of Cu/ZnO/Al_2O_3 Catalyst by Controlling its Precursor Structure, Green Energy & Environment, 2020, https://doi.org/10.1016/j.gee.2020.11.027 in press.
[14] Z. Sun, Y. Tian, P. Zhang, G. Yang, N. Tsubaki, T. Abe, A. Taguchi, J. Zhang, L. Zheng, X. Li, Sputtered Cu-ZnO/γ-Al_2O_3 bifunctional catalyst with ultra-low Cu content boosting dimethyl ether steam reforming and inhibiting side reactions, Ind. Eng. Chem. Res. 58 (2019) 7085–7709.
[15] J.P.S. Nascimento, A.C. Oliveira, J.C.S. Araujo, F.F. Sousa, G.D. Saraiva, E. Rodríguez-Aguado, E. Rodriguez-Castellon, Combined promoting effect of molybdenum on the bimetallic Al_2O_3-La_2O_3 catalysts for NO_x reduction by CO, Fuel 275 (2020), 117872.
[16] B. Seynnaeve, J. Lauwaert, P. Vermeir, P. Van Der Voort, A. Verberckmoes, Model-based control of iron- and copper oxide particle distributions in porous γ-Al_2O_3 microspheres through careful tuning of the interactions during impregnation, Mater. Chem. Phys. 276 (2021), 12542.
[17] A.P.S. Oliveira, I.S. Gomes, A.S.B. Neto, A.C. Oliveira, J.M. Filho, G.D. Saraiva, J. M. Soares, S. Tehuacanero-Cuapa, Catalytic performance of MnFeSi composite in selective oxidation of styrene, ethylbenzene and benzyl alcohol, Mol. Catal. 436 (2017) 29–42.
[18] A.P.S. Oliveira, I.S. Gomes, A.C. Oliveira, J.M. Filho, G.D. Saraiva, J.M. Soares, F. F. Sousa, A. Campos, Styrene oxidation to valuable compounds over nanosized FeCo-based catalysts: effect of the third metal addition, Catalysts 7 (2017) 323.
[19] J.V. do Carmo, A.C. Oliveira, J.C.S. Araujo, A. Campos, G.C.S. Duarte, Synthesis of highly porous alumina-based oxides with tailored catalytic properties in the esterification of glycerol, J. Mater. Res. 33 (2018) 1–9.
[20] S. Ishak, S. Mandal, H.-S. Lee, J.K. Singh, pH-controlled synthesis of sustainable lauric acid/SiO_2 phase change material for scalable thermal energy storage, Sci. Rep. 11 (2021) 5012.
[21] J.U. Maheswari, C. Krishnan, S. Kalyanaraman, P. Selvarajan, Growth and characterization of an organic nonlinear optical material—lauric acid crystal, Mater. Res. Express 3 (2016), 105101.
[22] S. Meghan, P. Kabra, S. Chakraborty, N. Padmavathy, Understanding the pathway of antibacterial activity of copper oxide nanoparticles, RSC Adv. 5 (2015) 12293–12299.

[23] R. Abazari, A.R. Mahjou, S. Sanati, Magnetically recoverable Fe_3O_4-ZnO/AOT nanocomposites: synthesis of a core–shell structure via a novel and mild route for photocatalytic degradation of toxic dyes, J.M.Liquids 223 (2016) 1133–1142.
[24] A. Pardakhty, M. Ranjbar, M.H. Moshafi, S. Abbasloo, A. Systemati, Study of ZnO/CuO core/shell nanostructures pegylated by microwave assistant reverse micelles (RM) method, J. Cluster Sci. 29 (2018) 1061–1068.
[25] R. Abazari, G. Salehi, A.R. Mahjou, Ultrasound-assisted preparation of a nanostructured zinc(II) amine pillar metal-organic framework as a potential sorbent for 2,4-dichlorophenol adsorption from aqueous solution, Ultrason. Sonochem. 46 (2018) 59–67.
[26] A.L. Lopes, M.B. Santos, A.J.S. Mascarenhas, L.A. Silva, Synthesis of CdS nanospheres by a simple and fast sonochemical method at room temperature, Mater. Lett. 136 (2014) 111–113.
[27] J.H. Adair, E. Suvaci, Submicron Electroceramic Powders by Hydrothermal Synthesis, Encyclopedia of Materials, Science and Technology, 2001.
[28] C.M.B. Santos, S.W. da Silva, L.R. Guilherme, P.C. Morais, SERRS study of molecular arrangement of amphotericin B adsorbed onto iron oxide nanoparticles precoated with a bilayer of lauric acid, J. Phys. Chem. C 115 (2011) 20442–20448.
[29] A. Sahaia, N. Goswamia, S.D. Kaushik, S. Tripathic, $Cu/Cu_2O/CuO$ nanoparticles: novel synthesis by exploding wire technique and extensive characterization, Appl. Surf. Sci. 390 (2016) 974–983.
[30] A.J. Reddy, M.K. Kokil, H. Nagabhushan, J.L. Rao d, C. Shivakumara, B. M. Nagabhushan, F.R.P.S. Chakradhar, Combustion synthesis, characterization and Raman studies of ZnO nanopowders, Spectrochim. Acta, Part A 81 (2011) 53–58.
[31] F. Silva Lisboa, J.E.F. C Gardolinski, C.S. Cordeiro, Fe.Wypych, layered metal laurates as active catalysts in the methyl/ethyl esterification reactions of lauric acid, J. Braz. Chem. Soc. 23 (2012) 46–56.
[32] P. Uznanski, J. Zakrzewska, F. Favier, S. Kazmierski, E. Bryszewska, Synthesis and characterization of silver nanoparticles from (bis)alkylamine silver carboxylate precursors, J Nanopart. Res. 19 (2017) 121.
[33] F. Silva Lisboa, J.E.F. C Gardolinski, C.S. Cordeiro, Fe.Wypych, layered MetalLaurates as active catalysts in the methyl/ethyl esterification reactions of lauric acid, J. Braz. Chem. Soc. 23 (2012) 46–56.
[34] P. Uznanski, J. Zakrzewska, F. Favier, S. Kazmierski, E. Bryszewsk, Synthesis and characterization of silver nanoparticles from (bis)alkylamine silver carboxylateprecursors, J Nanopart. Res. 19 (2017) 121.
[35] W. Kong, X. Fu, Y. Yuan, Z. Liu, L. Jingxin, Pereparation and thermal properties ofcrosslinkedpolyurethane/lauric acid composites as novel form stable phase change materials with a low degree of supercooling, RSC Adv. 7 (2017), 29554.
[36] A.N. da Silva, A.B.S. Neto, A.C. Oliveira, M.C. Junior, J.A.L. Junior, P.T.C. Freire, J. M. Filho, A.C. Oliveira, R. Lang, Raman studies of nanocomposites catalysts: temperature and pressure effects of CeAl, CeMn and NiAl oxides, Spectrochim. Acta Part A: Mol. Biomol.Spectrosc. 198 (2018) 160–167.
[37] S.M.B. Albahrani, G. Simon, S. Ayrinhac, M. Gauthier, F. Decremps, I. Lisiecki, S. Constanzo, P. Colomban, Stability of lauric acid at high pressure studied by Raman spectroscopy and picosecond acoustics, Eur. Phys. J. B 92 (2019) 35, https://doi.org/10.1140/epjb/e2018-90479-7.
[38] A.M. El-Toni, M.A. Habila, J.P. Labis, Z.A. ALOthman, M. Alhoshan, A. A. Elzatahryf, F. Zhang, Design, synthesis and applications of core–shell, hollow core, and nanorattle multifunctional nanostructures, Nanoscale 8 (2016) 2510.
[39] L.F. Oton, A.C. Oliveira, J.C.S. de Araujo, R.S. Araujo, F.F. de Sousa, G.D. Saraiva, R. Lang, L. Otubo, G.C. da Silva Duarte, A. Campos, Selective catalytic reduction of NO_x by CO (CO-SCR) over metal-supported nanoparticles dispersed on porous alumina, Adv. Powder Technol. 31 (2020) 464–476.
[40] C.I. Ezugwu, B. Mousavi, M.A. Asraf, Z. Luo, F. Verpoort, Post-synthetic modified MOF for Sonogashira cross-coupling and Knoevenagel condensation reactions, J. Catal. 344 (2016) 445–454.
[41] L. He, H. Cheng, G. Liang, Y. Yu, F. Zh, Effect of structure of $CuO/ZnO/Al_2O_3$ composites on catalytic performance for hydrogenation of fatty acid ester, Appl. Catal., A: GEN 452 (2013) 88–93.
[42] J.P.S. Nascimento, L.F. Oton, A.C. Oliveira, E. Rodríguez-Aguado, E. Rodríguez-Castellón, R.S. Araujo, M.S. Souza, R. Lang, Selective catalytic reduction of NO_x by CO over doubly promoted $MeMo/Nb_2O_5$ catalysts (me = Pt, Ni, or Co), Catalysts 10 (2020) 1048.
[43] F. Raimondi, K. Geissler, J. Wambach, A. Wokaun, Hydrogen production by methanol reforming: post-reaction characterisation of a $Cu/ZnO/Al_2O_3$ catalyst by XPS and TPD, Appl. Surf. Sci. 189 (2002) 59–71.
[44] S.U. Nandanwar, S. Rathod, V. Bansal, V.V. Bokade, A review on selective production of acetophenone from oxidation of ethylbenzene over heterogeneous catalysts in a decade, Catal. Lett. 7 (2021) 2116–2131.
[45] M. Salavati-Niasari, F. Davar, Synthesis, characterization, and catalytic oxidation of ethylbenzene over host (zeolite-Y)/guest (copper(II) complexes of tetraaza macrocyclic ligands) nanocomposite materials, J. Coord. Chem. 63 (2010) 3240–3255.
[46] R. Xie, G. Fan, L. Yang, F. Li, Hierarchical flower-like Co–Cu mixed metal oxidemicrospheres as highly efficient catalysts for selective oxidation of ethylbenzene, Chem. Eng. J. 288 (2016) 169–178.